Li et al. Nanoscale Research Letters (2015) 10:420
DOI 10.1186/s11671-015-1118-6

Nanoscale Research Letters
a SpringerOpen Journal

NANO REVIEW Open Access

# Conductance Quantization in Resistive Random Access Memory

Yang Li[1,2], Shibing Long[1,2*], Yang Liu[3], Chen Hu[3], Jiao Teng[3], Qi Liu[1,2], Hangbing Lv[1,2], Jordi Suñé[4] and Ming Liu[1,2*]

## Abstract

The intrinsic scaling-down ability, simple metal-insulator-metal (MIM) sandwich structure, excellent performances, and complementary metal-oxide-semiconductor (CMOS) technology-compatible fabrication processes make resistive random access memory (RRAM) one of the most promising candidates for the next-generation memory. The RRAM device also exhibits rich electrical, thermal, magnetic, and optical effects, in close correlation with the abundant resistive switching (RS) materials, metal-oxide interface, and multiple RS mechanisms including the formation/rupture of nanoscale to atomic-sized conductive filament (CF) incorporated in RS layer. Conductance quantization effect has been observed in the atomic-sized CF in RRAM, which provides a good opportunity to deeply investigate the RS mechanism in mesoscopic dimension. In this review paper, the operating principles of RRAM are introduced first, followed by the summarization of the basic conductance quantization phenomenon in RRAM and the related RS mechanisms, device structures, and material system. Then, we discuss the theory and modeling of quantum transport in RRAM. Finally, we present the opportunities and challenges in quantized RRAM devices and our views on the future prospects.

**Keywords:** Resistive random access memory (RRAM), Resistive switching (RS), Conductive filament (CF), Conductance quantization

## Review

### Introduction

The persistent perusing of massive storage volume has been driving the scaling-down process of memory devices for decades. Memories characterized by low-power consumption and low fabrication cost are needed. Predominant flash memory has met a scaling-down limitation around 10-nm magnitude [1, 2]. Therefore, intensive studies have been carried out in seeking for the next-generation memories. Resistive random access memory (RRAM) has become one of the most promising candidates for the next-generation memory [3–14] because of the intrinsic excellent scalability, simple metal-insulator-metal (MIM) structure, low fabrication cost, 3D integration feasibility, and promising performances in speed, power, endurance, retention, etc. RRAM stores information based on the resistive switching effect. Under appropriate external electrical field, the resistance state of the RRAM device can be reversibly switched between a high resistance state (HRS) or OFF-state and a low resistance state (LRS) or ON-state. There are two resistive switching modes, i.e., unipolar and bipolar switching operations under the same or opposite bias polarities, respectively, which are closely related to the different material systems and the different switching mechanisms. The resistive switching can be a uniform or localized phenomenon. Uniform switching proportionally scales with the total area of the switching material, while localized switching is usually based on the formation and disruption of conductive filament (CF).

Abundant resistive switching materials, electrode materials, and their various interfaces are involved in RRAM switching mechanisms which are rather complex. Rich electrical, thermal, magnetic, and optical effects are therefore presented. Typical physical/chemical effects accompanied in resistive switching processes and in HRS/LRS states include electrochemical/thermochemical reactions [15–27], metal-insulator transition [28, 29], magnetic modulation [30–47], etc. In this regard, the RRAM device can serve as a rich platform for studying the multiple physical/chemical effects. In the CF-type

* Correspondence: longshibing@ime.ac.cn; liuming@ime.ac.cn
[1]Key Laboratory of Microelectronics Devices and Integrated Technology, Institute of Microelectronics, Chinese Academy of Sciences, Beijing 100029, China
Full list of author information is available at the end of the article

Springer

© 2015 Li et al. **Open Access** This article is distributed under the terms of the Creative Commons Attribution 4.0 International License (http://creativecommons.org/licenses/by/4.0/), which permits unrestricted use, distribution, and reproduction in any medium, provided you give appropriate credit to the original author(s) and the source, provide a link to the Creative Commons license, and indicate if changes were made.

RRAM device, when the CF in the resistive switching (RS) layer is formed, RRAM changes to LRS. If the CF is ruptured, the device switches back to HRS. The formation and rupture of the CF can be understood as cation or anion migration under applied voltage companied by electrochemical reaction of the metal or oxygen vacancies. Therefore, CF is believed to be consisted of metal or oxygen vacancies. The dimension of the CF can be electrically modulated to be in the order of several tens to a few nanometers, which has been evidenced by the observation of high-resolution transmission electron microscopy (HRTEM) [20, 48–60], scanning TEM (STEM) [59], and atomic force microscopy (AFM) [61–63]. In the localized filamentary switching, the scaling down of the RRAM device [64] would not influence its memory characteristics until the area is approaching the CF magnitude. As the CF size is in the range of nanoscale to atomic size, which is comparable to the mean free path (Fermi wavelength) of conduction electron, the scattering might be absent, resulting in ballistic electron transport [65] and the quantized conductance (QC) [66–68]. In recent studies, conductance quantization phenomena have been proved to exist in the atomic-sized CF in RRAM [69–72], and the interest for studying them continues. Revealing the QC effect is of great significance to deeply understand the physics of RS mechanism in mesoscopic dimension, which is important to control the performance, reliability, and variability [73, 74] of RRAMs and to advance their practical application as non-volatile memories. At the same time, if the conductance quantization behaviors can be well modulated, it in turn can be utilized to realize the multi-level storage for ultra-high-density memory applications. Thus, summarizing and discussing the QC effect in RRAM is very necessary. In this review paper, we focus our attention on the recent development of the research on the QC effect in CF-based non-volatile RS devices including basic QC phenomenon in RRAM, RS mechanisms, device structures, materials, theory, and modeling of conductance quantization in RRAM.

## Operating Principles and RS Mechanism of RRAM

In RRAM cell with MIM structure, non-volatile data storage is achieved through the reversible resistive switching between HRS and LRS, which are utilized to store the digits "0" and "1." RS is often based on the creation and partial destruction of CF. Dependent on the polarity of the external electrical field, RS is usually classified into two modes, unipolar and bipolar switching. The transition from HRS to LRS and that from LRS to HRS are called as the SET and RESET switching, respectively. In some cases, if the prepared RS layer in fresh cell is very insulating with low amount of defects, a forming process with high voltage is necessary to soft breakdown the RS layer to trigger the subsequent reproducible RESET and SET switching. Figure 1 shows the schematic *I*–*V* curves in RS and the corresponding states of CF-type RRAM device.

Compared with the prototypical non-volatile memories (NVMs) such as magnetic random access memory (MRAM) based on the giant or tunneling magnetoresistance effect [75–79] and phase change random access memory (PRAM) based on the reversible phase transitions between amorphous and crystalline states of phase change materials [80–84], RRAM, an emerging NVM, has shown various complex resistive switching mechanisms, which is closely dependent on the different types of switching layer and electrode materials and also dependent on the different operation methods [85–87]. To date, the resistive switching mechanism in RRAM has been widely accepted to be mainly attributed to the reduction/oxidation (redox) electrochemistry mechanism, which can operate in the bulk RS layer, along CFs in the RS layer, and/or at the RS layer/metal contact interfaces in the MIM structure. Redox-based RRAM [3, 15, 19, 88–95] can be further classified into two main types, "nanoionic" (including electrochemical metallization (ECM) [17–20, 90, 94, 96–101] and valence change mechanism (VCM) [5, 51, 61, 91, 102–112]) and "thermochemical mechanism (TCM)" (i.e., fuse/antifuse) [91, 113, 114]. In ECM and VCM devices, the diffusion or drift of charged species ($Ag^+$ or $Cu^+$ cations), O anions or oxygen vacancies (Vos) in the RS layer are driven by the ion drift/redistribution and the redox electrochemistry mechanisms under an electrostatic drift field. While in TCM devices, it is driven by a thermal gradient diffusion mechanism. In fact, in a practical RRAM device, the RS process is very complicated, with multiple mechanisms simultaneously existing, but a certain one is predominant. It is worth pointing out that TCM is sometimes confused with unipolar VCM. In some cases, the ECM device is also called as conductive bridge random access memory (CBRAM) [115–119], programmable metallization cell (PMC) [120–122], and atomic switch [115–119, 123, 124]. If TCM dominates the RS, the resistance switching is unipolar. On the contrary, if ECM or VCM is dominant, the switching is usually bipolar. ECM devices are cation migration-based RRAMs, while VCM and TCM devices can be summed up into anion migration-based RRAMs. Plenty of dielectric materials have been found to show the redox-based resistance switching effect, including perovskites, solid-state electrolytes, chalcogenides, transition metal oxides, silicon dioxide, metal nitrides, organic complexes, polymers, etc., among which $HfO_2$ and $TaO_x$ are most widely investigated and most competitive for the practical applications. Table 1 lists the three types of typical redox-based RS mechanisms and their corresponding material system, *I*–*V* curves, and operation polarity.

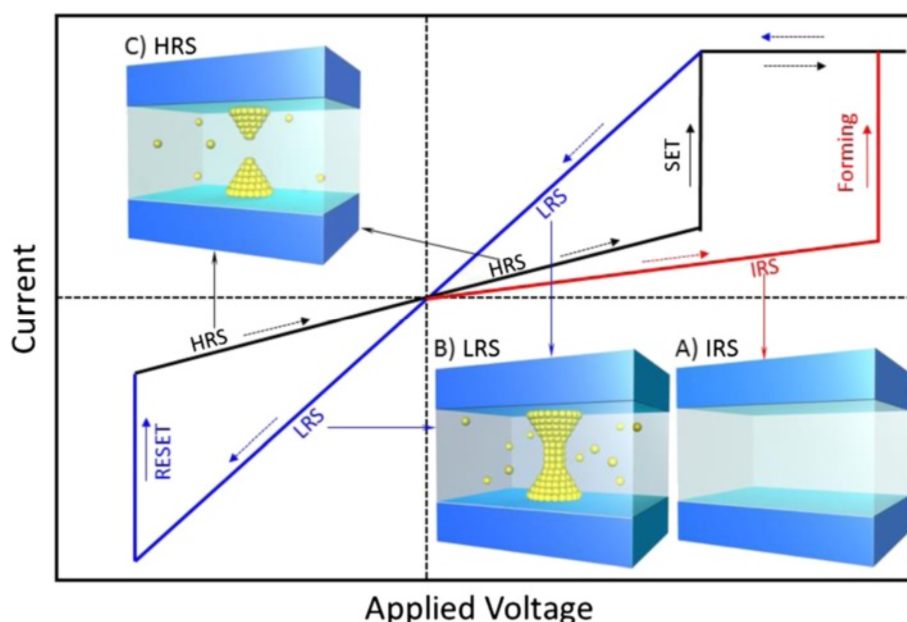


**Fig. 1** Schematic *I*–*V* curves of resistive switching process in a CF-type bipolar RRAM device. Insets *A*–*C* show the different resistance states of the device during the switching process. In most cases, the fresh RRAM device shows a very high initial resistance state (IRS) with few defects (inset *A*). In a positive bias sweep, when the voltage increases to a comparative high voltage ($V_{Forming}$), the device switches to the low resistance state (LRS) with a conducting filament formed in the RS layer (inset *B*). Then, in a negative voltage sweep, when the voltage reaches a critical value ($V_{RESET}$), the device switches from LRS to the high resistance state (HRS), corresponding to a RESET transition in which the CF is ruptured (inset *C*). At last, in another positive sweep, the device will switch to LRS again, with the filament reconnected (inset *B*). This process is called as SET, with the SET voltage ($V_{SET}$) much lower than ($V_{Forming}$). If the device has a good endurance, the above SET and RESET switching can be reproducibly and successively carried out for a large number of cycles

Except the redox RS mechanism, the insulator-metal transition (IMT) or Mott transition in MIM structure can also contribute to RS effect. The corresponding resistive switching device is called as Mott memory and sometimes referred as correlated electron random access memory (CeRAM). In this type of memory device, the charge injection under the external electrical field induces the transition from weakly correlated electron state to strongly correlated electron state, which is activated by a critical electron population [125–127]. Electronic switches and memory elements based on the Mott transition have been explored using several typical material systems involved in Mott memory including $VO_2$ [128, 129], NiO [126, 127, 130], $SrTiO_3$ [131], $SmNiO_3$ [132], etc. The quasi two-dimensional electron gas (2DEG) formed at the interface between complex oxides has also been reported to show the metal-insulator transition effect [133–136]. However, in this paper, we will focus on the redox-based filamentary RS mechanisms that have been shown to support the conductance quantization effect.

## Conductance Quantization in RRAM

The size of the CF can be modulated to the range of nanoscale to atomic size in both RESET and SET process. The modulation process can be achieved through specific electrical operations, especially in the RRAM devices showing progressive RESET/SET behavior [137]. This is similar to the performance of memristor [6, 138–142]. When CF is controlled to be thin enough to show atomic size, the quantum-sized effect [69] will appear in the CF-type RRAM devices. Conductance quantization phenomenon is an important representation of quantum-sized effect. Figure 2 gives an example of conductance quantization behavior observed in RRAM. The measured current–voltage (Fig. 2a) and corresponding conductance-voltage curves (Fig. 2b) show that the conductance quantization phenomenon appears in the RESET process of a $Pt/HfO_2/Pt$ unipolar RRAM device. Obvious quantized conductance steps with multiples of $G_0$ can be observed, in other words, abrupt conductance transitions of the order of $G_0$ between well-defined discrete states can be found in the final stages of the RESET transient. $G_0 = 2e^2/h$ is the quantum of conductance, with the value of $12.9\ \text{k}\Omega^{-1}$ or $77.5\ \mu\text{s}$, where $e$ is the electron charge and $h$ is Planck's constant. Quantized conductance observed in the practical materials usually presents fluctuation with a certain degree, so statistical analysis on plenty of experimental data is often made use of to intrinsically reveal

**Table 1** The classification of redox-based resistive switching mechanisms and operation principles of redox-based RRAM

| Switching mechanism | Electrochemical metallization (ECM) | Valence change mechanism (VCM) | Thermochemical mechanism (TCM) |
|---|---|---|---|
| Dominating charged species | Metal cations | O anions or oxygen vacancies (Vo) | O anions or oxygen vacancies (Vo) |
| Intrinsic nature of CF | Metal CF | Vo-CF (bipolar) | Vo-CF (unipolar) |
| Dominating driving force | External electric field | External electric field | Thermal gradient |
| Primary operation principle | SET process: (1) The active TE material (Ag, Cu, Ni) in the interface is oxidized under positive electric field; (2) the cations ($Ag^+$, $Cu^+$ or $Cu^{2+}$, $Ni^+$) drift into the RS layer; (3) the cations are reduced back from the BE/RS-layer interface or from the bulk RS layer or even from the TE/RS layer, depending on the difference between the drift velocity of cations and electrons; (4) metal CF is formed to connect BE and TE, with the reduction process continuing. | SET process: (1) Under positive electric field, TE material in the TE/RS-layer interface is oxidized and $O^{2-}$/Vo is generated; (2) O ions drift to TE or O vacancies drift to BE through the RS layer to form Vo-CF. The valence states of corresponding cations are changed. | SET (antifuse) process: O vacancies are generated, diffused, and redistributed to form Vo-CF in the bulk RS layer under the thermal gradient induced by electric field. The valence states of corresponding cations are changed. |
| | RESET process: Under the opposite electric field, the metal atoms in the CF are oxidized and drift away, thus CF is partially ruptured. | RESET process: Under the opposite electric field, O ions migrate back to the bulk RS layer to recombine with O vacancies in the CF, thus CF is partially ruptured. | RESET (fuse) process: CF is ruptured or fused as a result of joule heating along the CF through the thermal diffusion process of O vacancies. |
| Typical RS materials | Ion-conducting solid electrolyte (sulfides, selenides, or telluride of Ge, As, Sb, or Ga) such as $Ag_2S$ [53], GeSe [224], $Cu_2S$ [172, 225], $Ag_2Se$ [226], Ag-Ge-Se [227], $(AgI)_{0.5}(AgPO_3)_{0.5}$ [228], etc.; Binary or complex oxides such as $HfO_2$ [215, 222, 229, 230], $ZrO_2$ [231, 232], $SiO_2$ [233], $WO_3$ [234], $TaO_x$ [235], $GdO_x$ [236], etc. | Transition metal oxides (TMOs) such as $TiO_2$ [51, 87], $HfO_2$ [106], $ZrO_2$ [112], $SrTiO_3$ [5, 61], $TaO_x$ [102], $WO_3$ [111], etc.; doped $SiO_2$ [104, 107–109]; amorphous C [103, 105, 110], etc. | Transition metal oxides (TMOs) such as $HfO_2$ [69, 70, 216, 237], NiO [22, 238–244], CoO [245], CuO [246], $Fe_2O_3$ [247], etc. |
| Typical electrode materials | (1) Top electrode (TE): an electrochemically active metal such as Ag, Cu, and Ni. | (1) Top electrode (TE): a low work function metal not easily reduced back after oxidation, such as Ti, Al, and Nb. | (1) Top electrode (TE): inert electrodes such as Pt, Pd, Ir, Ru, W, Au, etc. |
| | (2) Bottom electrode (BE): an electrochemically inert counter electrode such as Pt, Pd, Ir, Ru, W, Au, etc. | (2) Bottom electrode (BE): inert electrodes, such as Pt, Pd, Ir, Ru, W, Au, etc. | (2) Bottom electrode (BE): inert electrodes such as Pt, Pd, Ir, Ru, W, Au, etc. |
| Dominating material | Electrode | RS layer and electrode | RS layer |

**Table 1** The classification of redox-based resistive switching mechanisms and operation principles of redox-based RRAM *(Continued)*

| | | | |
|---|---|---|---|
| Typical *I–V* curve | 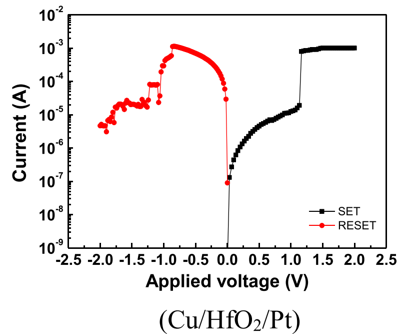<br>(Cu/HfO$_2$/Pt) | 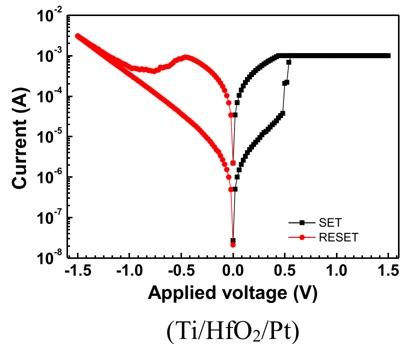<br>(Ti/HfO$_2$/Pt) | 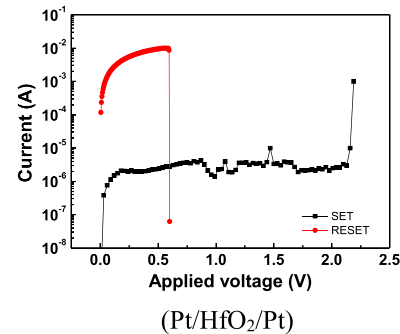<br>(Pt/HfO$_2$/Pt) |
| Operation polarity | Bipolar | Bipolar | Unipolar |
| RS type | Localized | Localized | Localized |

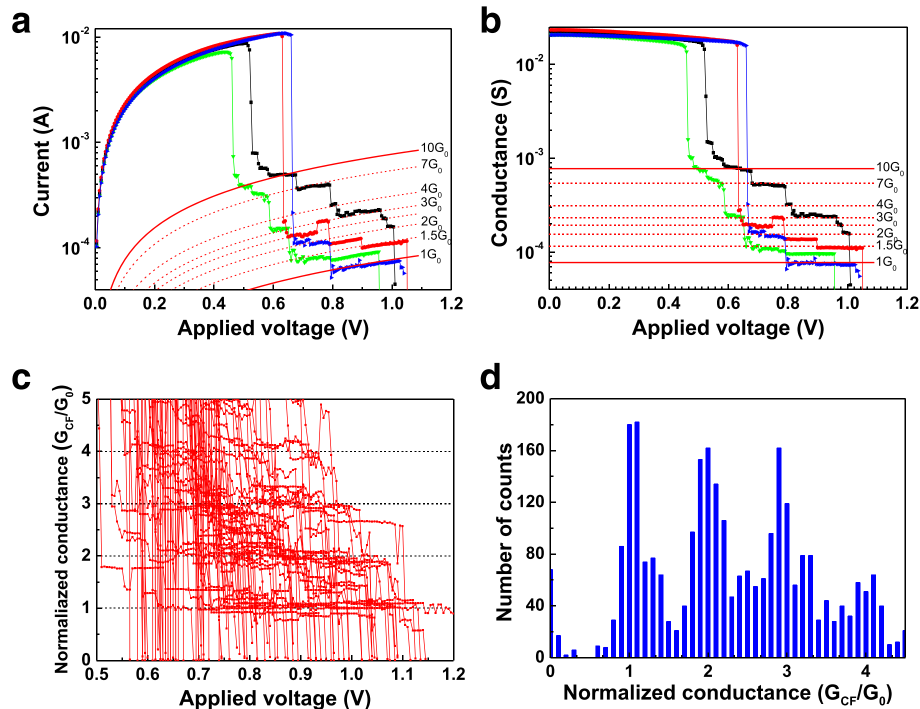


**Fig. 2** Conductance quantization phenomenon measured in the RESET process of a Pt/$HfO_2$/Pt unipolar RRAM device. **a** $I-V$ curves in four RESET cycles. **b** $G-V$ curves corresponding to (**a**). $G$ is defined as $I/V$. The RESET transients of the device show discrete states with half-integer multiples of the conductance quantum. The *red lines* in (**a**) and (**b**) are "guides to the eye" and correspond to $I = nG_0V$ or $G = nG_0$ with $n = 1$, 1.5, 2, 2.5, 3, 4, 7, and 10. Discrete conductance levels at about 1 $G_0$, 1.5 $G_0$, 2 $G_0$, 2.5 $G_0$, 3 $G_0$, 4 $G_0$, etc. are evident. **c** Evolution of CF conductance in the last stage of 100 successive RESET switching cycles of the Pt/$HfO_2$/Pt device. Discrete conductance levels at 1 $G_0$, 2 $G_0$, 3 $G_0$, 4 $G_0$, etc. are revealed. **d** Histogram of normalized conductance collected at the step-like gradual RESET phase in 100 successive RESET cycles. Conductance peaks at integer and semi-integer multiples of $G_0$ are clearly present

this effect. Figure 2c further shows the evolution of CF conductance of this device in the last stage of 100 successive RESET switching cycles. By collecting the conductance data at the step-like gradual RESET phase in the 100 successive RESET cycles in Fig. 2c, we can plot the histogram of normalized conductance, as shown in Fig. 2d. Conductance levels and peaks at 1 $G_0$, 2 $G_0$, 3 $G_0$, 4 $G_0$, etc. are clearly displayed in Fig. 2c, d, respectively.

Only the size of a conductor is small enough will the quantized conductance effect appear. In fact, as pointed out by Datta, if any of the three dimensions of a conductor is smaller than one of the three characteristic length scales [143]: (1) de Broglie wavelength of electrons; (2) the mean free path of electrons; and (3) the phase-relaxation length of electrons, the conductor will show conductance quantization behavior. Figure 3 shows the typical ranges of the three characteristic length in metal and semiconductor materials. In the devices with atomic-scale CF, the CF configuration is determined by the atomic granularity of the material. In this case, the transport through the CF is governed by the quantum nature of conductance, i.e., the current is carried along the discrete conductance channels. The reason for the occurrence of conductance quantization is that the electrons are not scattered when transporting through the atomic-scale conductor. The conductor behaves like a waveguide for electrons and does not follow the Ohm's law anymore. The waveguide could be understood as a ballistic transportation path made up of a bundle of discrete conductance channels, with each contributing a maximum amount of one $G_0$ to the total conductance of the conductor. The total conductance of the conductor is described by the Landauer formula, $G = G_0\Sigma_i T_i$ [144]. $T_i$ is the transmission probability of each discrete conductance channel. If the channel is assumed to be fully transmitted, $T_i$ equals to one. $T = \Sigma_i T_i$ is the transmission probability of the whole conductor, which is determined by the details of the conductor geometry and the electronic structure of the conductor material [145].

In fact, the phenomenon of quantum conductance was first observed by Van Wees et al. in a two-dimensional electron gas of a GaAs-AlGaAs heterostructure in 1988 [146]. Similar results were reported almost simultaneously by Wharam et al. [147], also using a 2D electron gas on a GaAs-AlGaAs heterojunction, at 0.1 K. Since

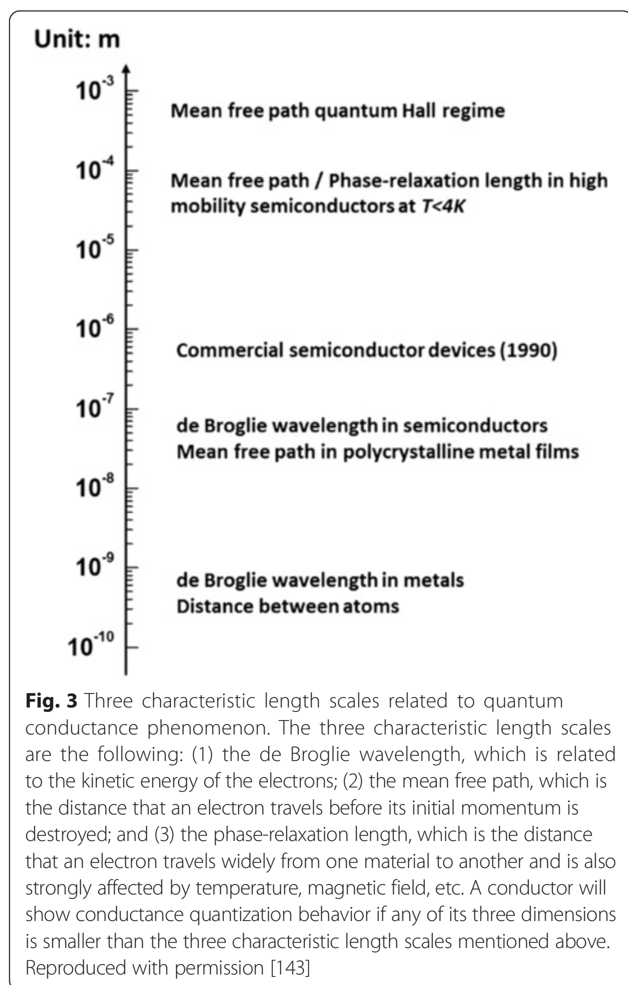


**Fig. 3** Three characteristic length scales related to quantum conductance phenomenon. The three characteristic length scales are the following: (1) the de Broglie wavelength, which is related to the kinetic energy of the electrons; (2) the mean free path, which is the distance that an electron travels before its initial momentum is destroyed; and (3) the phase-relaxation length, which is the distance that an electron travels widely from one material to another and is also strongly affected by temperature, magnetic field, etc. A conductor will show conductance quantization behavior if any of its three dimensions is smaller than the three characteristic length scales mentioned above. Reproduced with permission [143]

then, the phenomenon of quantized conductance has been reported in various physical structures such as atomic quantum contact [68, 146, 148–155], mechanically controllable break junctions [156–160], nanotubes [161–167], and the current-induced local oxidation of nanoscale constrictions [168].

As conductance quantization effect in RRAM has the potential applications of multi-level storage, it has attracted much attention in recent years. Conductance quantization phenomena were initially found in ECM devices [169] and then in VCM and TCM devices [69, 170, 171]. Conductance quantization effect in RRAM has been studied and reported in a series of literatures [69, 70, 126, 127, 129, 137, 140, 170–190], involving various materials and different RS mechanisms, CF types, SET, or RESET processes, as listed in Table 2. Some typical experimental observation results are given below as illustrations for quantum conductance phenomenon, as shown in Figs. 4, 5, 6, 7, and 8 [70, 171, 183, 186, 191].

The quantized conductance state of CF is practically an intermediate state or a specific LRS state with the conductance ($G$) in the order of $G_0$, i.e., integer multiples of $G_0$. One $G_0$ can be simply understood as being corresponding to a single atomic point contact or a nanowire. Conductance quantization effect indicates that the evolution of CF can be modulated to be in units of single atomic point contacts.

## Structures, Materials, and Operation Methods of RRAM with QC Effect

There are many observations and reports of quantum conductance phenomenon in RRAM. Different device structures, switching and electrode materials, and operating methods are applied. They are summarized respectively as follows.

### *Device Structures*

The basic structure of RRAM is a thin resistive switching layer, which is usually nanometers in thickness, sandwiched between two electrodes. Many derivative structures have been fabricated based on this basic structure. There are three kinds of structures of RRAM device exhibiting conductance quantization effect, as shown in Fig. 9. Figure 9a [171] shows a commonly used sandwich RRAM structure. It is a stack of thin films of bottom electrode, RS layer, and patterned top electrode. Figure 9b [180] shows a crossbar structure. Figure 9c [170] shows a structure similar to those in Fig. 9a, b, with the only difference being that a tip, such as a conductive atomic force microscopy (CAFM) tip, is used as the top electrode. More detailed fabrication information is not given here for it is not the main point of this paper.

### *Material Systems*

Since the quantized conductance phenomenon is the property of nanoscale conductors, the materials of RRAM devices especially those consisting of the CF play an important role to the quantized conductance behaviors. As has been discussed in "Introduction" section, the types of RS and electrode materials determine resistive switching mechanisms for the filament-based RRAM. For ECM devices, resistive layer is sandwiched between an inert electrode and an active electrode. During the forming and SET process, the metal ions of the active electrode are driven into the resistive layer, forming the CF. For VCM devices, both top and bottom electrode are inert and the CF is consisted of oxygen vacancies. So as for the ECM mechanism, the material of the active electrode is critical for the observation of the quantized conductance, while for the VCM mechanism, the material of the resistive layer plays a more important role.

In fact, the papers on conductance quantization in RRAM were initially published in 1991. Hajto et al. reported their observation of conductance quantization of RRAM for the first time. The studied device structure

**Table 2** Different material systems showing conductance quantization effect

| System | RS mechanism | CF | Quantization level | RS polarity | QC observed in SET or RESET |
|---|---|---|---|---|---|
| $Ag_2S$ or $Cu_2S$ (vacuum gap) [169] | ECM | Ag | $G_0$ | Bipolar | SET |
| Ag/AgI/Pt [180] | ECM | Ag | $G_0$ | Bipolar | SET |
| Ag/$SiO_2$/Pt [195, 213] | ECM | Ag | 0.5 $G_0$ | Bipolar | SET |
| Ag/$Ta_2O_5$/Pt [181] | ECM | Ag | $G_0$ | Bipolar | SET and RESET |
| Ag/$Ag_2S$/Pt (STM tip) [182] | ECM | Ag | $G_0$ | Bipolar | RESET |
| Ag/$P_3$HT:PCBM/ITO [183] | ECM | Ag | $G_0$/0.5 $G_0$ | Bipolar | SET and RESET |
| Ag/a-$La_{1-x}Sr_xMnO_3$/Pt [185] | ECM | Ag | $G_0$ | Bipolar | SET |
| Ag/ionic conductor-layer/W tip [191] | ECM | Ag | $G_0$ | Bipolar | SET |
| Ag/$GeS_2$/W [193] | ECM | Ag | $G_0$ | Bipolar | SET |
| Cr/$p^+$-amorphous silicon/V [192] | ECM | Metal | 0.5 $G_0$ | Unipolar | SET |
| Nb/$ZnO_x$/Pt [170] | ECM | Nb or Vo | $G_0$/0.5 $G_0$ | Bipolar | SET and RESET |
| Cu/$HfO_x$/Pt [190] | ECM | Cu | 0.5 $G_0$ | Bipolar | SET |
| Pt/$HfO_2$/Pt [69] | VCM | Vo | 0.5 $G_0$ | Unipolar | RESET |
| ITO/$ZnO_x$/ITO [170] | VCM | Vo | 0.5 $G_0$ | Unipolar | SET and RESET |
| Ti (Ta, W)/$Ta_2O_5$/Pt [171] | VCM | Vo | $G_0$ | Bipolar | SET and RESET |
| V/$V_2O_5$/V [174] | - | - | 0.5 $G_0$ | - | SET |
| W/$CeO_x$/$SiO_2$/$NiSi_2$ [179] | VCM | Vo | 0.5 $G_0$ | Bipolar | RESET |
| n-Si/$SiO_x$/p-Si [186] | VCM | Vo | $G_0$/0.5 $G_0$ | Bipolar and Unipolar | SET |
| Ti/$HfO_2$/TiN [188] | VCM | Vo | $G_0$ | Bipolar | RESET |
| Ti/$TiO_2$/$SrTiO_3$/n-Si [194] | VCM | Vo | $G_0$ | Bipolar | SET |

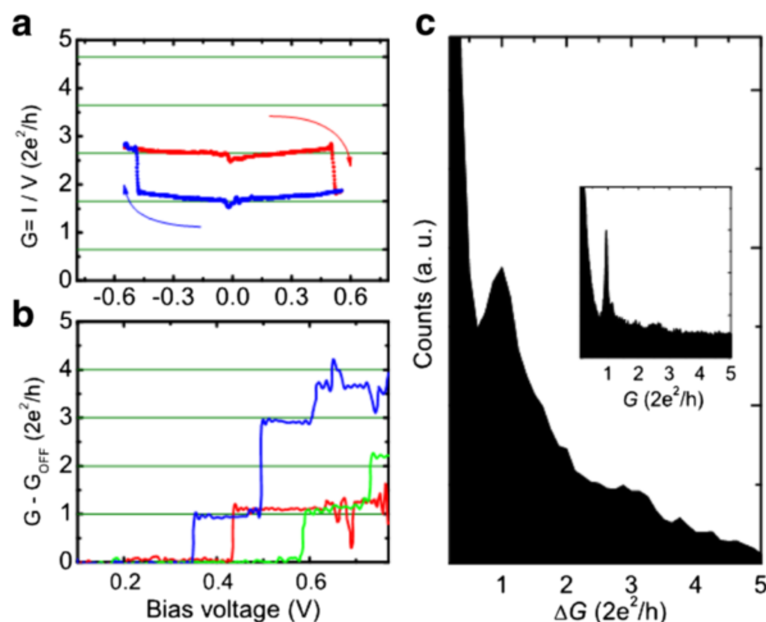


**Fig. 4** Switching characteristics and conductance quantization observed in nanoscale junctions with a structure of tungsten tip/ionic conductor layer/silver film [191]. **a** Conductance change during SET and RESET operation which shows atomic-scale conductance switching. *Green lines* act as guides to the eye representing a series of conductance levels with equal interval of 1 $G_0$. **b** Conductance change from high resistance state to low resistance state following voltage sweep for three independent conductance states. **c** Histogram of the conductance difference between high resistance states and the low resistance states during the voltage sweep. The histogram consists of 130 independent $I-V$ curves with initial ON-state conductance smaller than 10 $G_0$. $\Delta G$ is the difference between the conductance and the zero-bias conductance. The inset histogram shows 5000 repeated and closing cycles at a constant bias voltage of 100 mV. Reproduced with permission

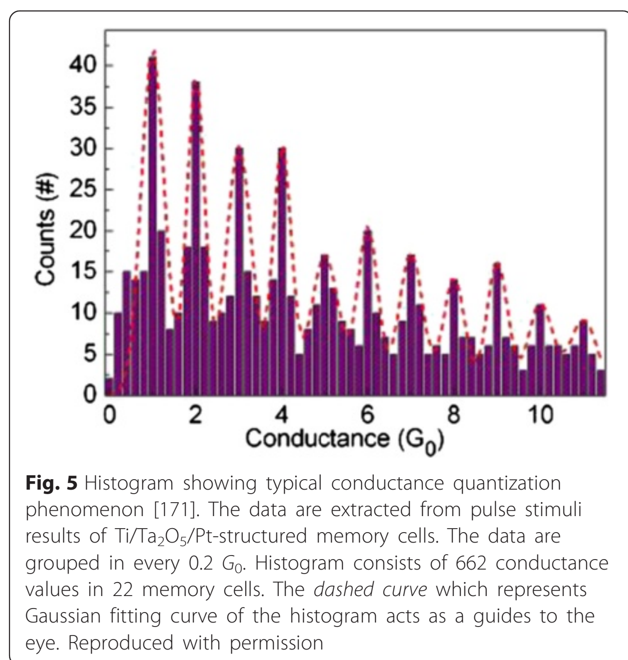


**Fig. 5** Histogram showing typical conductance quantization phenomenon [171]. The data are extracted from pulse stimuli results of Ti/$Ta_2O_5$/Pt-structured memory cells. The data are grouped in every 0.2 $G_0$. Histogram consists of 662 conductance values in 22 memory cells. The *dashed curve* which represents Gaussian fitting curve of the histogram acts as a guides to the eye. Reproduced with permission

is Cr/α-Si:H/V [192]. Yun et al. showed similar result in the V/α-$V_2O_5$/V [174] device. Quantized conductance effect was observed in cation migration-based RRAMs [172, 173] and then extended to anion migration-based RRAMs [69, 70, 133, 169, 170]. Since 2012, conductance quantization has attracted a lot of attention, mainly for its potential applications in the multi-level storage, and also for its interesting physics behind the phenomena. As a result, conductance quantization has been reported in more and more RRAM devices, as shown in Table 2. It should be noted that the reports of conductance quantization in sandwich structures with a vacuum gap [169] or a scanning tunneling microscope (STM) tip [170] are also included in this table.

In most cases of ECM RRAMs with QC effect, the reported material for active electrode is Ag [169, 180–183, 185, 191, 193]. Besides Ag, Nb [170] and V [174] have also been reported to be able to form quantum conductors in RRAM. The RS materials involving QC effect include traditional solid-state electrolyte materials such as AgI [180], $Ag_2S$ [169, 182], $Cu_2S$ [169], $GeS_2$ [193], and transition metal oxides, such as $Ta_2O_5$ [171, 181], $LaSrMnO_3$ [185], α-Si [192], and polymer [183]. In bipolar and unipolar VCM devices with QC effect, the reported resistive switching material includes silicon oxide [186], transition metal oxides, such as $HfO_2$ [69, 188], $Ta_2O_5$ [171, 181], $ZnO_x$ [170], etc., and bi-layered oxides, such as $TiO_2/SrTiO_3$ [194] and $GeO_x/SiO_2$ [179]. Among the reported RS materials which exhibit conductance quantization, $Ta_2O_5$ [171, 181] and $HfO_2$ [69, 188] show good performances irrespective of the type of the CFs, i.e., Vo-CF or metal CF. Both ECM and VCM devices made up of $HfO_2$ and $Ta_2O_5$ materials have shown obvious QC effect, as shown in Figs. 2, 5 [171], and 8 [70].

It can be seen from Table 2 that most reported devices show conductance step with integer multiples of $G_0$, while in some material systems, the conductance variation step may be half-integer multiples of $G_0$. The explanation of this difference will be discussed later in "Theory and Modeling of Quantum Transport in RRAM" section.

### *Operating Methods*

To successfully observe the QC effect in RRAMs, it is of importance to make use of appropriate operating methods to the devices to accurately control the size of CFs to be close to the atomic scale. In this section, we will deal with all kinds of reported operating methods, including fresh device operation, voltage sweeping,

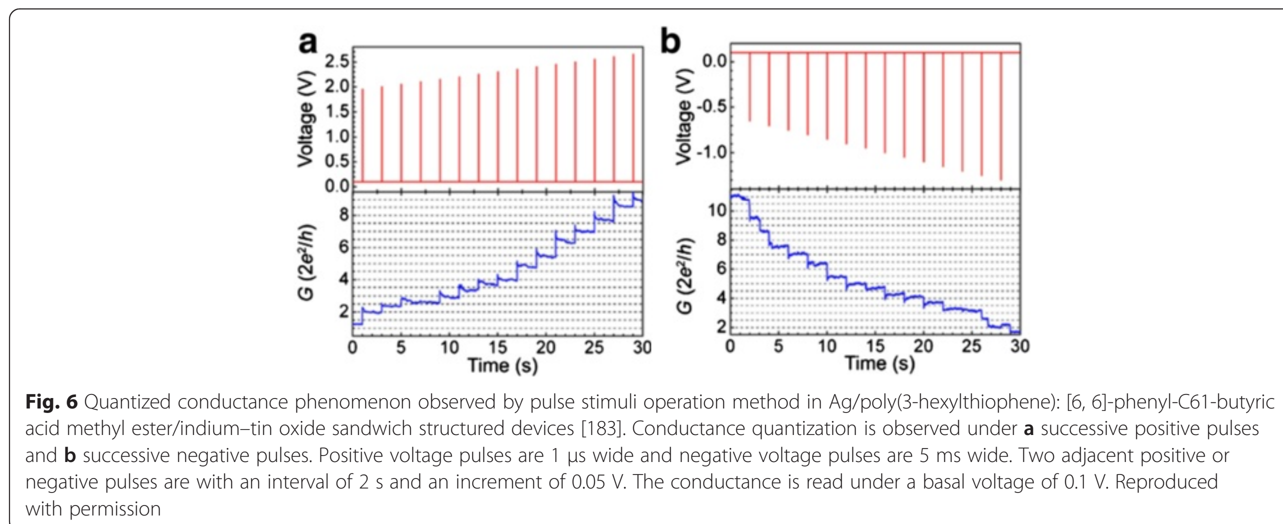


**Fig. 6** Quantized conductance phenomenon observed by pulse stimuli operation method in Ag/poly(3-hexylthiophene): [6, 6]-phenyl-C61-butyric acid methyl ester/indium–tin oxide sandwich structured devices [183]. Conductance quantization is observed under **a** successive positive pulses and **b** successive negative pulses. Positive voltage pulses are 1 μs wide and negative voltage pulses are 5 ms wide. Two adjacent positive or negative pulses are with an interval of 2 s and an increment of 0.05 V. The conductance is read under a basal voltage of 0.1 V. Reproduced with permission

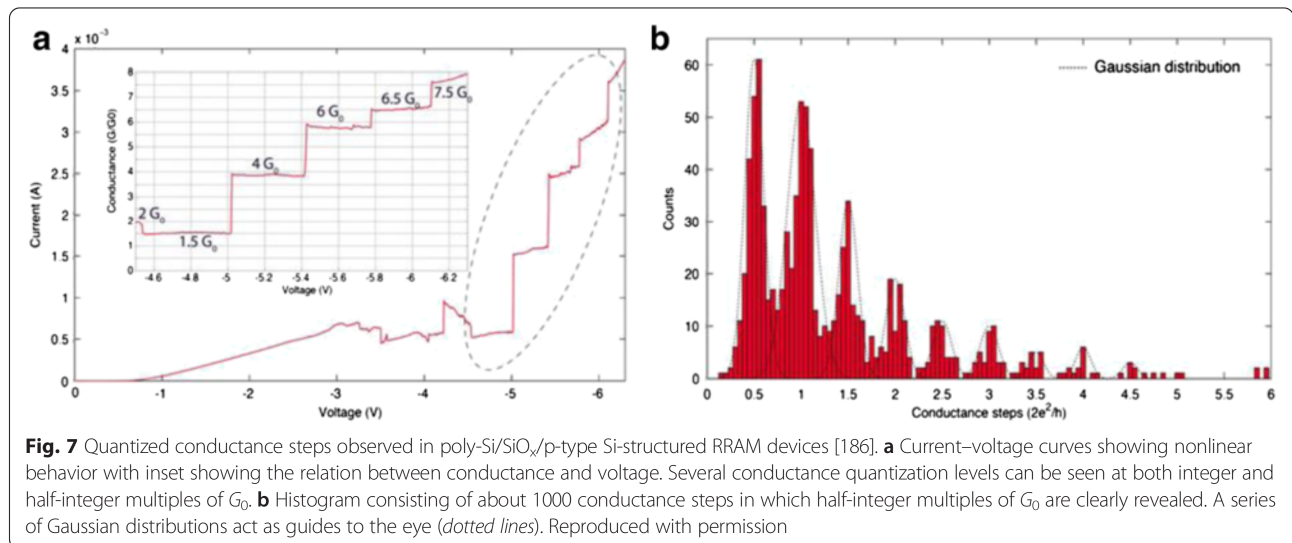


**Fig. 7** Quantized conductance steps observed in poly-Si/$SiO_x$/p-type Si-structured RRAM devices [186]. **a** Current–voltage curves showing nonlinear behavior with inset showing the relation between conductance and voltage. Several conductance quantization levels can be seen at both integer and half-integer multiples of $G_0$. **b** Histogram consisting of about 1000 conductance steps in which half-integer multiples of $G_0$ are clearly revealed. A series of Gaussian distributions act as guides to the eye (*dotted lines*). Reproduced with permission

voltage pulse operation, current sweeping, and constant voltage bias operation.

**Fresh Device Operation** Before analyzing the detailed operation methods to achieve QC effect, we need to first discuss the different operating conditions for the RRAM devices with different initial resistance states (IRS). For the fresh RRAM devices, most of them show an initially very high resistance state and a forming operation is needed to form CF in the resistive layer. Since the fresh resistive layer is usually in high resistance state, a much higher voltage, compared with the SET process, is needed to form the CF in the resistive layer, as shown in Fig. 10a [170]. Compared to the forming process, the

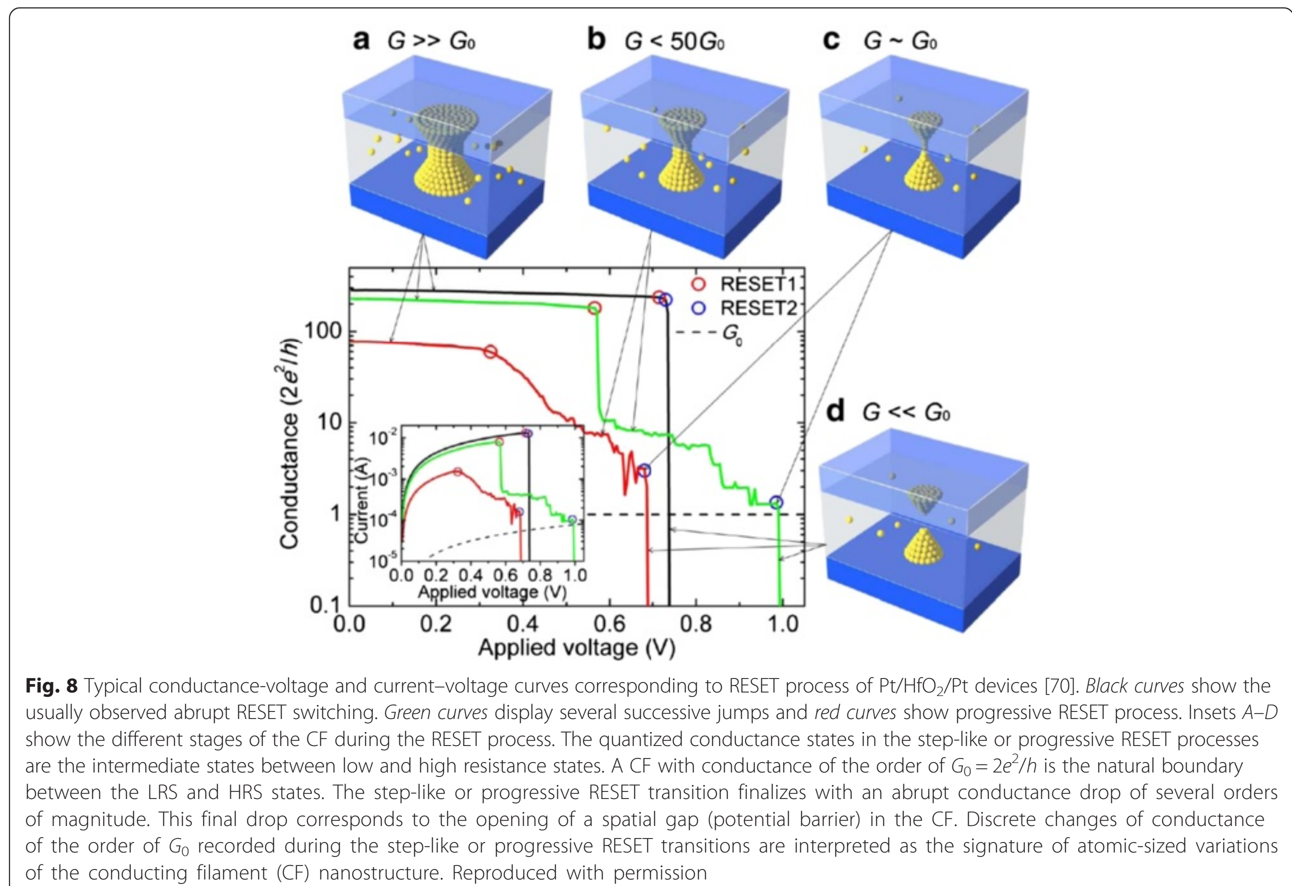


**Fig. 8** Typical conductance-voltage and current–voltage curves corresponding to RESET process of Pt/$HfO_2$/Pt devices [70]. *Black curves* show the usually observed abrupt RESET switching. *Green curves* display several successive jumps and *red curves* show progressive RESET process. Insets *A–D* show the different stages of the CF during the RESET process. The quantized conductance states in the step-like or progressive RESET processes are the intermediate states between low and high resistance states. A CF with conductance of the order of $G_0 = 2e^2/h$ is the natural boundary between the LRS and HRS states. The step-like or progressive RESET transition finalizes with an abrupt conductance drop of several orders of magnitude. This final drop corresponds to the opening of a spatial gap (potential barrier) in the CF. Discrete changes of conductance of the order of $G_0$ recorded during the step-like or progressive RESET transitions are interpreted as the signature of atomic-sized variations of the conducting filament (CF) nanostructure. Reproduced with permission

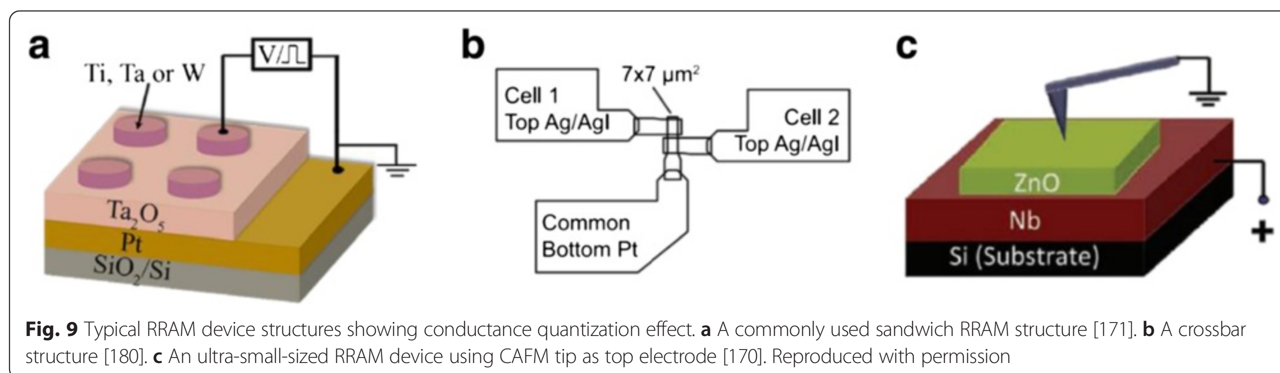


**Fig. 9** Typical RRAM device structures showing conductance quantization effect. **a** A commonly used sandwich RRAM structure [171]. **b** A crossbar structure [180]. **c** An ultra-small-sized RRAM device using CAFM tip as top electrode [170]. Reproduced with permission

voltage amplitude applied in the SET process is lower, because the CF formed in the forming process will not be dissolved completely in the successive RESET operation, thus a lower voltage can program the device. But for some RRAMs, the forming process and the SET process show no obvious difference, i.e., the characteristics of the device in initial fresh state and high resistance state have no clear distinction, as shown in Fig. 10b [179]. In other words, this kind of RRAM device has the free-forming characteristics. Some RRAM devices also possibly show an initial low resistance state. For example, in the quantized conductance atomic

**Fig. 10** Typical forming, SET, and RESET characteristics of fresh RRAM devices with different initial resistance states. **a** Switching process illustration of Nb/ZnO/Pt device with an initial high resistance state [170]. Higher voltage in forming is needed compared to that in the SET process. **b** Switching process illustration of a free-forming $p^+Si/NiSi_2/SiO_2/CeO_x/W$ device [179]. The Forming process and the SET process show no obvious difference. **c** Schematic illustration of $Ag_2S$-based QCAS device and switching behavior between OFF- and ON-state [169]. The initial state of the device is ON-state and a RESET process is needed to start the switching cycles. Reproduced with permission

switch (QCAS), as shown in Fig. 10c [169], it is initially in the ON-state. To start the switching cycles, the device needs to be RESET at first under a certain positive voltage bias. Due to the large amount of Ag atoms to be ionized to incorporate into the $Ag_2S$ crystal in this first RESET process, the switching time of this process is quite long, lasting for a few seconds. But after this initial RESET operation, the device can work quickly with a high operation frequency of 1 MHz.

**Voltage Sweeping Mode** After the initial process which involves forming/SET, RESET or no particular operation method to start switching cycles, a certain operation method is needed to switch the device between ON-state and OFF-state. The most common operation method is voltage sweeping mode. The voltage sweeping in SET process induces electrochemical reactions resulting to the formation of CF. The voltage sweeping in RESET process contributes to joule-heating-assisted oxidation followed by the diffusion of metal ions or oxygen vacancies (Vo) under the concentration gradient and the applied electric field [181]. Many experimental results [69, 170, 171, 179, 180, 188] showing conductance quantization under voltage sweeping mode have been reported. Figure 11 shows some of the reported experimental results in different device structures. Figure 11a [188] shows the progressive RESET process of the Ti/$HfO_2$/TiN-structured devices which exhibit bipolar RS behaviors. In the inset of Fig. 11a, zoomed current and voltage relation is shown and several current jumps which indicates the conductance quantization could be clearly seen. Figure 11b [170] shows the conductance change in bipolar characterized Nb/ZnO/Pt devices as a function of the bias voltage during the SET process. At

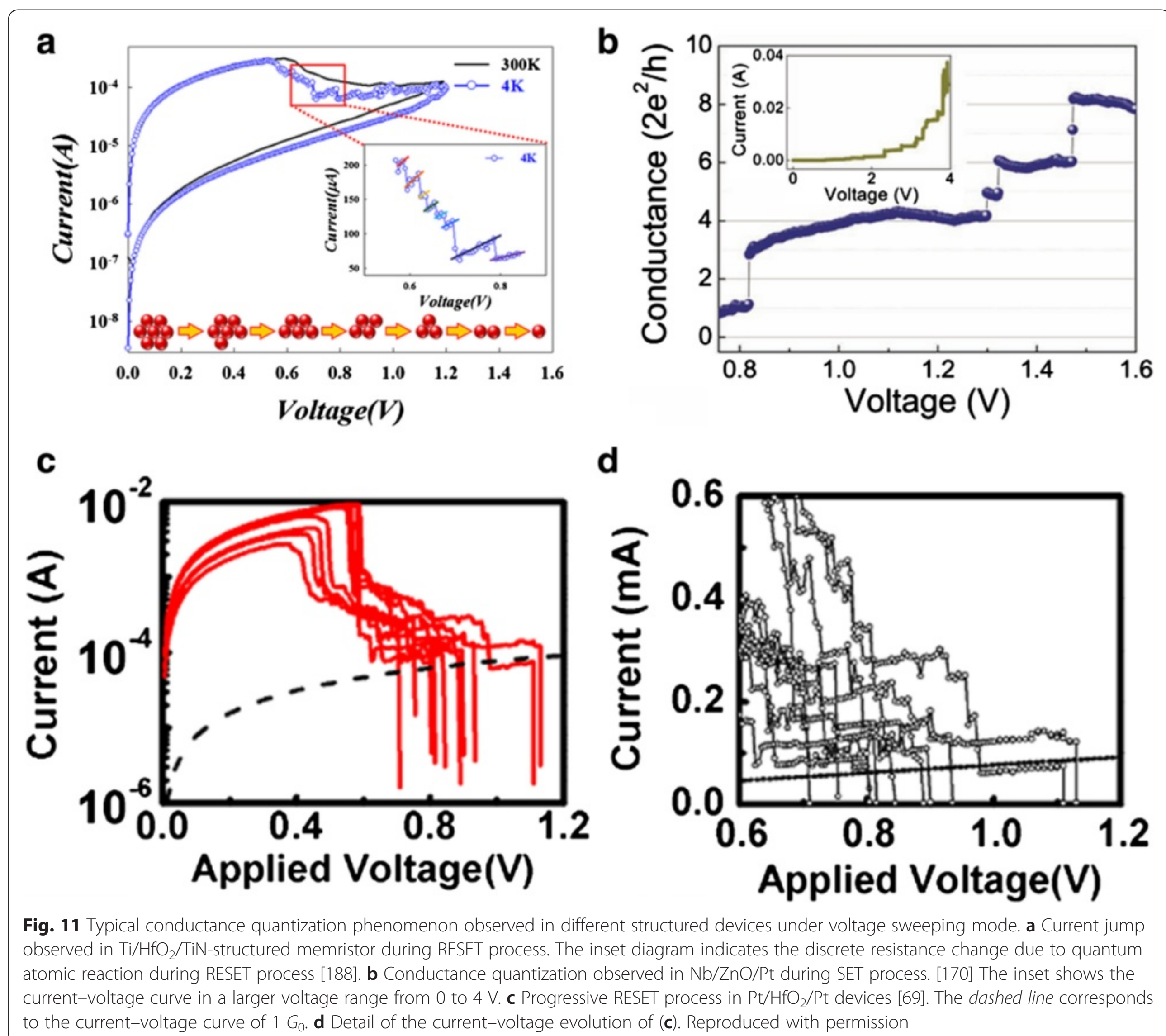


**Fig. 11** Typical conductance quantization phenomenon observed in different structured devices under voltage sweeping mode. **a** Current jump observed in Ti/$HfO_2$/TiN-structured memristor during RESET process. The inset diagram indicates the discrete resistance change due to quantum atomic reaction during RESET process [188]. **b** Conductance quantization observed in Nb/ZnO/Pt during SET process. [170] The inset shows the current–voltage curve in a larger voltage range from 0 to 4 V. **c** Progressive RESET process in Pt/$HfO_2$/Pt devices [69]. The *dashed line* corresponds to the current–voltage curve of 1 $G_0$. **d** Detail of the current–voltage evolution of (**c**). Reproduced with permission

least four conductance jumps are shown in the Fig. 11b and the conductance changed at a step of the integer multiples of quantum conductance $G_0$ from 1 to 8 $G_0$. The inset of Fig. 11b shows the current–voltage curve in a larger voltage range from 0 to 4 V. Figure 11c, d [69] shows the current–voltage curves in the RESET process of the unipolar Pt/$HfO_2$/Pt devices. Figure 11d shows the detail of Fig. 11c during the last phase of the RESET transients. The dash line in Fig. 11c corresponds to the current–voltage curve of a conductance of 1 $G_0$.

**Voltage Pulse Operation Mode** By applying appropriate pulse voltage, the conductance state of the RRAM device could be changed at steps of quantum conductance. Both ECM and VCM RRAMs show quantized conductance step change under voltage pulse operation, as shown in Figs. 12 [181] and 13 [171], respectively. For voltage pulse operation method, three parameters could be tuned, including the pulse amplitude, pulse width, and time interval between two adjacent voltage pulses.

Take Ag/$Ta_2O_5$/Pt RRAM as an example. Figure 12 shows the QC effect observed in this device. Under the pulse operation mode, the switching speed of the device is of the magnitude of μs to ns which is related to the values of the high resistance and the input pulse. The switching time is much shorter than the reaction time of the current compliance function, which results in the ineffectiveness of the current compliance function and leads to the further growth of the CF even after the current reaches the value of the compliance current. The solution for this problem is to insert a 3 kΩ resistor in series with the RRAM device, as shown in the inset of Fig. 12a. The current is limited by a 3 kΩ resistor during the stage that the RRAM switches from high resistance state to low resistance state. It is very important to limit the current value when the SET transition occurs. If there is no current limitation, the conductance of the device will abruptly jump to about 20 $G_0$, which indicates that the formed filament is rather thick and robust and quantized conductance step disappears. As can be seen from Fig. 12a, the quantized conductance increases from 0 to 9 $G_0$ at a step of conductance quantum under a series of increasing pulses from 0.3 to 0.7 V at a step of 0.05 V with time intervals of 2 s. Negative pulses with the same pulse width and interval time from −0.1 to −0.5 V were applied after the successive positive voltage pulses. In the negative pulse operation which corresponds to the RESET process, no series resistor is needed since the current in the circuit will decrease as the resistance value of RRAM increases in the RESET process. Similar quantized conductance change behavior has also been reported in the VCM RRAM with a structure of Ti/$Ta_2O_5$/Pt, as shown in Fig. 13.

The quantized conductance states change not only depending on the amplitude of the pulses but also depending on the time interval of the adjacent pulses. As shown in Fig. 14 [181], successive pulses with sufficiently long interval do not obviously change the conductance state. Whereas at short interval, pulses of the same amplitude and width make the conductance temporarily increase and gradually reach a constant value of $G_0$.

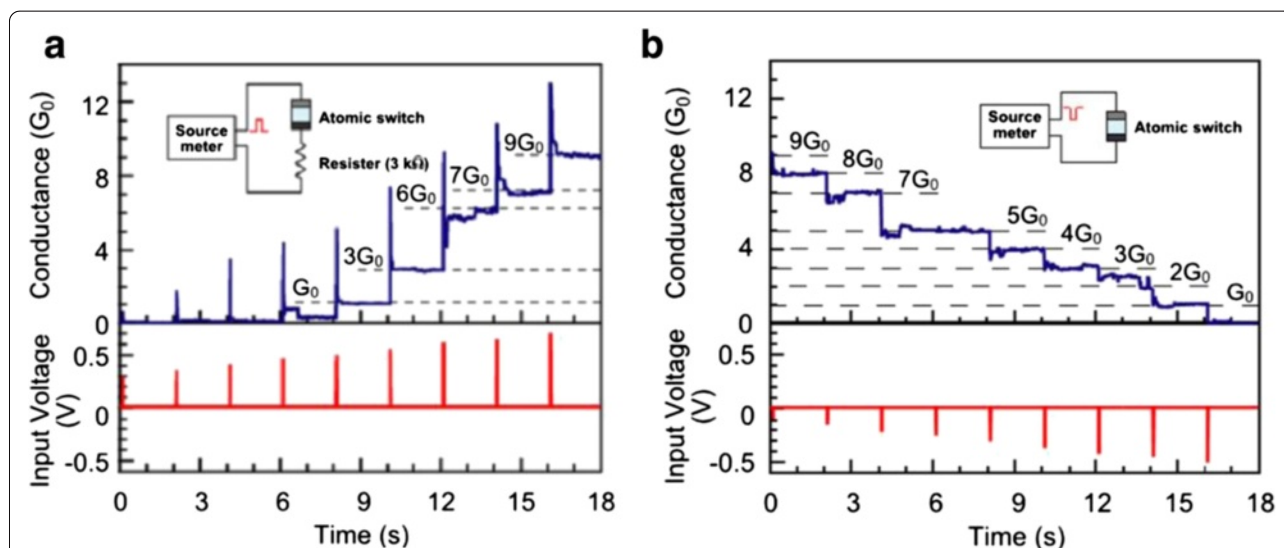


**Fig. 12** Quantized conductance observed in Ag/$Ta_2O_5$/Pt-structured ECM devices under voltage pulse operation mode [181]. **a** The value of conductance increases at steps of integer multiples of conductance quantum $G_0$ in the SET process under positive pulses with a width of 20 ms at an interval of 2 s. In order to prevent hard breakdown of RRAM device, a current-limiting resistor of 3 kΩ was connected in series with the device. **b** Quantized conductance decrease phenomenon observed in the RESET process under reversed voltage polarity. No current-limiting resistor is needed in the negative pulse stimuli mode. Reproduced with permission

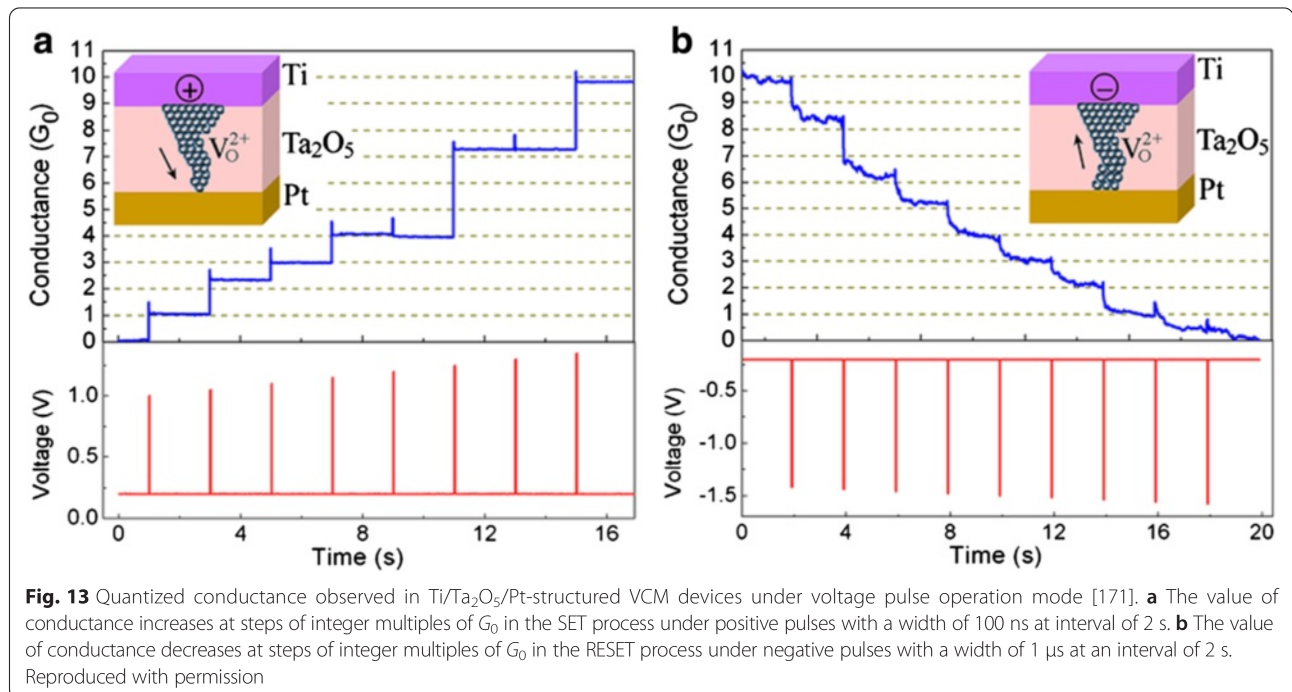


**Fig. 13** Quantized conductance observed in $Ti/Ta_2O_5/Pt$-structured VCM devices under voltage pulse operation mode [171]. **a** The value of conductance increases at steps of integer multiples of $G_0$ in the SET process under positive pulses with a width of 100 ns at interval of 2 s. **b** The value of conductance decreases at steps of integer multiples of $G_0$ in the RESET process under negative pulses with a width of 1 μs at an interval of 2 s. Reproduced with permission

**Current Sweeping Mode** In some material systems, no more than one or two discrete conductance drops could be detected by conventional voltage sweep operation. Current sweep mode is utilized as an alternative operation mode. Through this method, more discrete conductance levels could be observed, as shown in Fig. 15 [180, 195]. The different quantization evolution behavior in SET process by taking voltage sweep mode and current sweep mode comes from the different formation process of the CF. In the voltage sweep mode, stepwise increased voltage is applied to the device. As the voltage increases to the SET point, the filament forms and the resistance of the device suddenly drops to a much lower value. This leads to an abrupt current jump and the switching time is faster than the response time of the current compliance current which causes a further

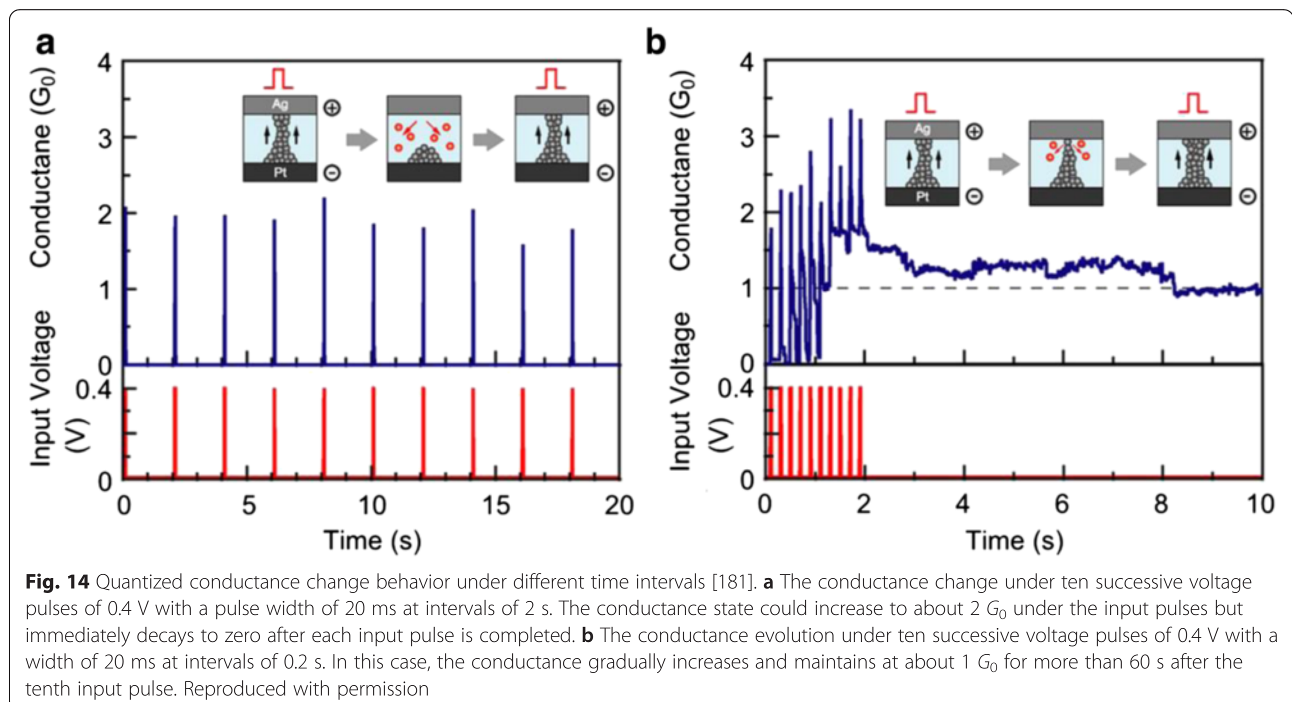


**Fig. 14** Quantized conductance change behavior under different time intervals [181]. **a** The conductance change under ten successive voltage pulses of 0.4 V with a pulse width of 20 ms at intervals of 2 s. The conductance state could increase to about 2 $G_0$ under the input pulses but immediately decays to zero after each input pulse is completed. **b** The conductance evolution under ten successive voltage pulses of 0.4 V with a width of 20 ms at intervals of 0.2 s. In this case, the conductance gradually increases and maintains at about 1 $G_0$ for more than 60 s after the tenth input pulse. Reproduced with permission

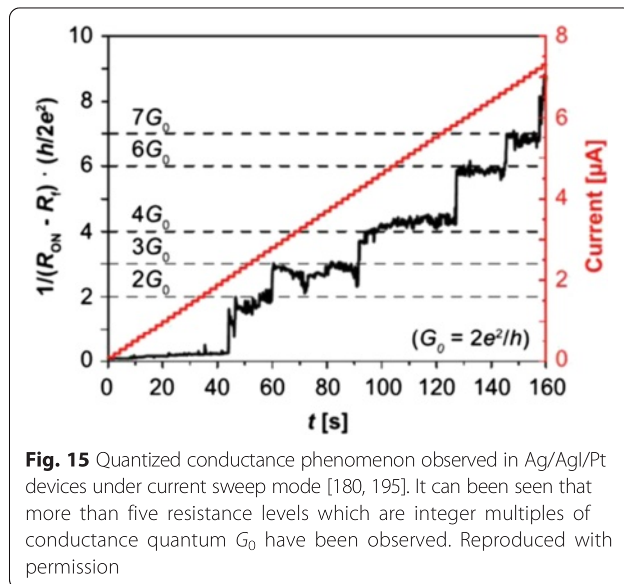


**Fig. 15** Quantized conductance phenomenon observed in Ag/AgI/Pt devices under current sweep mode [180, 195]. It can been seen that more than five resistance levels which are integer multiples of conductance quantum $G_0$ have been observed. Reproduced with permission

growth of CF after the SET point. Both voltage and current increase at the SET point which results in a positive feedback to the CF formation, thus leading to a very fast CF formation process. Whereas in the current sweep mode, the current is programmed to increase stepwise. At the SET point, the voltage dropped across the device decreases abruptly, due to the sudden decrease of the device's resistance. This leads to a negative feedback to the CF formation, so the CF formation process is more gradual than that under voltage sweep. In this case, more discrete conductance levels could be observed.

**Constant Voltage Bias Mode** Constant voltage bias is another way to observe quantized conductance. The bias value of voltage is critical to the observation of conductance quantization phenomenon. If the voltage amplitude is too large, the device may easily break down or the switching time may be too short to detect. On the other hand, if the amplitude of bias voltage is too small, the switching time of the device may be too long which is time consuming to observe conductance quantization or even no switching behavior could be observed, since the voltage is too small to drive the switching action to occur. Therefore, an appropriate bias voltage amplitude is needed for the observation of conductance quantization phenomenon, as shown in Figs. 16 [181] and Fig. 17 [69].

### Theory and Modeling of Quantum Transport in RRAM

Systems whose dimensions are much larger than microscopic objects like atoms but smaller than macroscopic objects are called mesoscopic systems [196]. When the dimension of the conductor is comparable to or smaller than the electron mean free path (mesoscopic scale), the

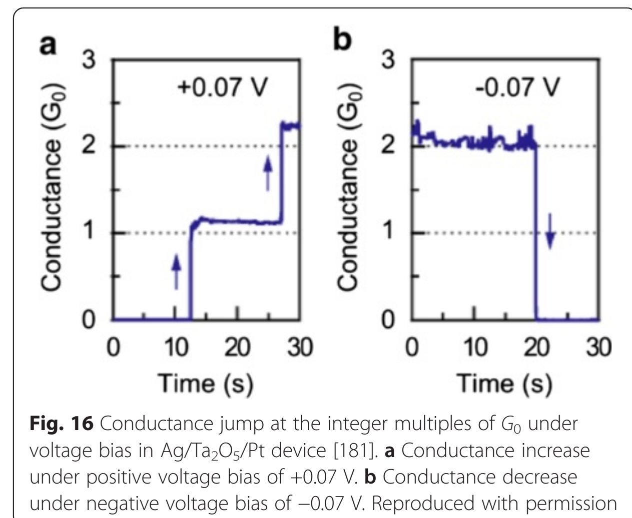


**Fig. 16** Conductance jump at the integer multiples of $G_0$ under voltage bias in $Ag/Ta_2O_5/Pt$ device [181]. **a** Conductance increase under positive voltage bias of +0.07 V. **b** Conductance decrease under negative voltage bias of −0.07 V. Reproduced with permission

classical Ohmic transport mechanism breaks down. When the conductor is under sufficiently high voltage, the Ohm's law does not apply for it either. When the above two conditions are satisfied, ballistic transportation begins to be dominant and the conductor behaves as an electron waveguide [197]. When the transmission probability $T$ for the waveguide equals one, this waveguide or conduction channel contributes an amount of $G_0$ to the total conductance of the mesoscopic conductor.

The theory of electron transport mechanism in mesoscopic systems exhibiting quantized conductance has been gradually established through a time span of decades from the suggestion of the prototype by Rolf Landauer in 1957 [198] to the publication of the book "Electronic Transport in Mesoscopic Systems" by Datta in 1995 [143]. Many theoretical calculations about

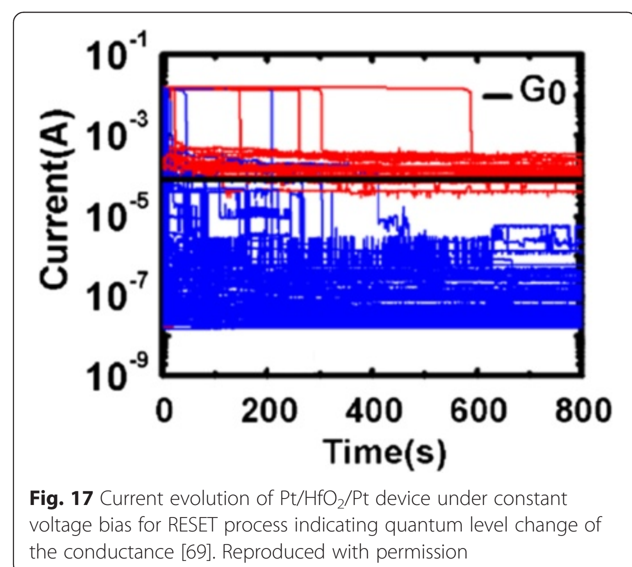


**Fig. 17** Current evolution of $Pt/HfO_2/Pt$ device under constant voltage bias for RESET process indicating quantum level change of the conductance [69]. Reproduced with permission

quantum conductance using different models have been reported [197, 199–209]. The quantized conductance steps were obtained in numerical and analytical calculations in a wide variety of materials [144, 205, 206, 208–211]. Review articles summarizing quantized conductance phenomenon in atomic-sized conductors [148] and nanowires [149] have also been published. At the same time, many experiments were also carried out to study quantized conductance [148, 156, 162, 163]. The conductance quantization effect was first observed in ballistic point contacts in the 2DEG of high-mobility GaAs-AlGaAs heterostructures in 1988 by Van Wees et al. [146], as shown in Fig. 18.

In RRAM, many theoretical works concerning calculation and simulation were reported. Several models have been proposed to describe and calculate the ballistic transportation and conductance quantization phenomenon in RRAM devices. As mentioned above, two conditions, i.e., small conductor dimension and high voltage bias, lead to ballistic transportation and conductance quantization, so in all proposed models, either the CF in resistive layer has been considered an atomic-sized conductor in insulator or the most constrictive part in CF is treated as being of atomic size. In this section, we will summarize four models. In the first one, the CF formed in the resistive layer is regarded as a one-dimensional linear atomic chain [175]. The second model treated the narrowest part of a CF as an atomic contact and calculated the electrical transport based on Landauer theory [179, 186, 212]. The third model focuses on CFs consisted of oxygen vacancies and calculated the quantized conductance of the filament with different space of oxygen vacancies through first principle calculation [69]. The fourth model is a circuit model, which ascribes the quantized conductance of the atom point contact in the ECM device to the discharge of the thermal emf voltage [195, 213].

### *One-Dimensional Linear Atomic Chain Model*

In the work of Jameson et al. [175], a model based on one-dimensional metal atomic chains was proposed to relate to the quantized conductance phenomenon and to calculate the programming time of RRAM device whose resistance tends to be programmed to integer multiples of fundamental conductance $G_0$ under sufficiently high currents. This model is different from other previous models which considered the filament as a bulk-like (although small) object whose resistance is continuous and proportional to the bulk resistivity.

In this model, the filament is simply treated as a linear chain of atoms, with the conductance in the order of $G_0$. A schematic illustration of the model is shown in Fig. 19. The CF is assumed to form from cathode to anode since the metal cations are usually reduced at the cathode. The resistive layer where the CF is formed is treated as a one-dimensional series of $N_w$ potential wells with a uniform height $V_i$ and width $d_i$ ("$i$" for internal). The last atom of the metal atom chain corresponds to the surface of the cathode. The resistive layer where CF is not

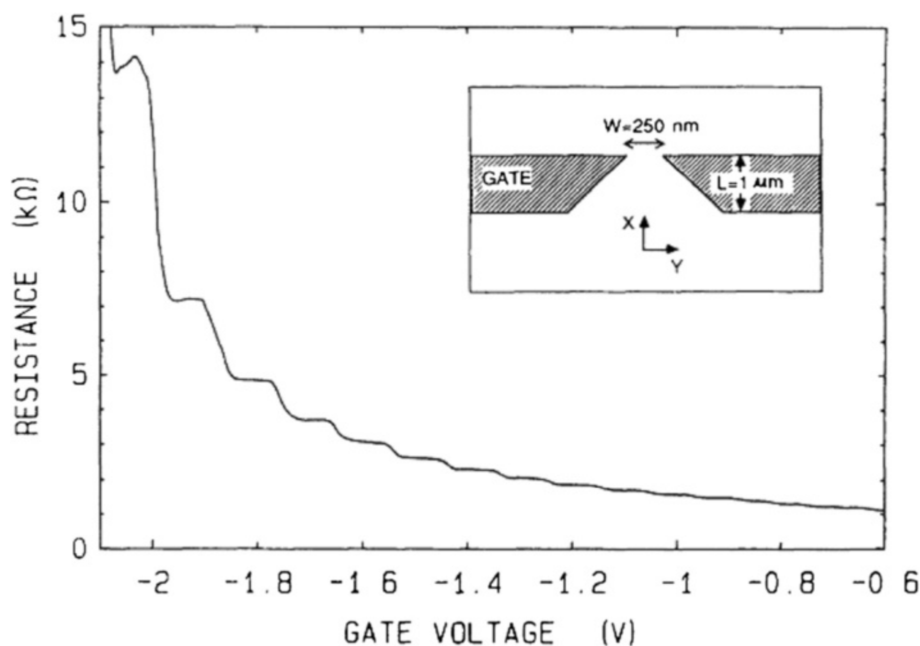


**Fig. 18** First observation of conductance quantization by Van Wees et al. [146]. The resistance of the point contact is a function of gate voltage at 0.6 K. The electron gas under the gate is depleted at −0.6 V when electrons only transport through the point contact and the contact is fully pinched off at −2.2 V. The inset shows the layout of the point contact. Reproduced with permission

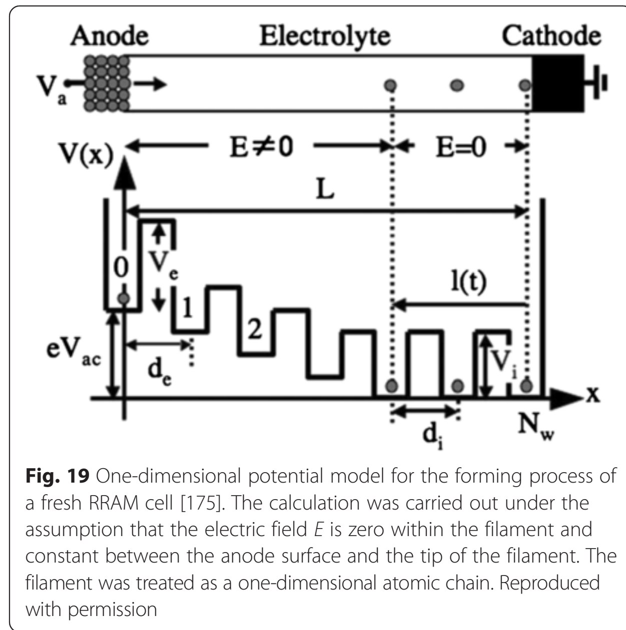


**Fig. 19** One-dimensional potential model for the forming process of a fresh RRAM cell [175]. The calculation was carried out under the assumption that the electric field $E$ is zero within the filament and constant between the anode surface and the tip of the filament. The filament was treated as a one-dimensional atomic chain. Reproduced with permission

formed yet is treated as a bulk electrolyte, and the resistive layer is separated by an "emission" barrier of height $V_e$ and width $d_e$ ("$e$" for emission) from the anode surface. When the positive forming or SET voltage $V_{\mathrm{ac}}$ is applied to the anode, the emission well is raised to an energy of $eV_{\mathrm{ac}}$, while the well $N_{\mathrm{w}}$ is kept at zero. A metal ion with a charge of $+e$ (e.g., $Ag^+$ for $Ag/GeS_2/W$ cells) will be emitted from anode into the potential well by thermal excitation over the emission barrier. Then, it travels through the periodic potential barriers which represent the resistive layer with no CF inside and stacks up against the cathode to promote the stretch of the CF, i.e., an atomic chain that grows with time. When all $N_{\mathrm{w}}$ wells are filled with metal ions, the resistance state of RRAM will suddenly switch to low resistance state and the time needed is the programming time of the device.

The programming time ($t_p$) of a RRAM cell whose resistance tends to increase to the integer multiple of $G_0$ was calculated. It was found that several intrinsic material parameters, including $V_{\mathrm{e}}$, $d_i$, $W_a - W_c$ (the difference between the work functions of the anode and cathode), influence the programming time of the virgin $Ag/GeS_2/$ W cells. After selecting proper values for these parameters, the model can nicely describe the dependence of $t_p$ on voltage, temperature, and $GeS_2$ thickness (for thick layers), which is in close relation to the quantization of the ON-state conductance. The model is effective for the cases of both constant voltage and ramped voltage programming. Further experimental study of the conductance quantization was reported by the same group in $Ag/GeS_2/W$ RRAM device afterwards [193] and the result is listed in Table 2.

### *Quantum Point Contact Model*

To deal with the post-breakdown (BD) conduction of gate dielectric of field effect transistor (FET), Suñé and Miranda have established the quantum point contact (QPC) model [214]. Recently, it has been found that the QPC model can be also made use of to describe the conduction of high and low resistance state in RRAM [71, 179, 182, 212, 215–219]. This model treats the thinnest part of the CF as a quantum point contact. It is able to explain the conductance quantization phenomenon in RRAM. The schematic illustration of the QPC model is shown in Fig. 20 [212]. The thinnest part of the CF is made up of a few atoms (Fig. 20a) and modeled as a potential barrier with several quantized subbands.

In the CF described by the QPC model, it was demonstrated that the Schrodinger equation can be decomposed into the transverse and longitudinal equations. Then, the quantum transport through a 3D tube-like constriction becomes a simple 1D tunneling behavior. The dispersion curve of the electronic subbands could be expressed as:

$$E(k_z, z) = \epsilon_n(z) + \frac{\hbar^2 k_z^2}{2m} \tag{1}$$

where $z$ and $k_z$ are the coordinates in the longitudinal direction in real-space and $k$-space, respectively, $m$ is the mass of the electron, and $\hbar$ is the reduced Planck constant. If the confinement is in a rectangle shape, then [202]

$$\epsilon_n(z) = \frac{\pi^2 \hbar^2}{2m} \left( \frac{n_x^2}{L_x(z)^2} + \frac{n_y^2}{L_y(z)^2} \right), \tag{2}$$

where $L_x(z)$ and $L_y(z)$ are the dimension of the constriction and $n_x$ and $n_y$ are integers. It means that the dispersion curve ($E - k_z$ relationship) consists of discrete parabolic subbands in each $z$, as shown in Fig. 20b. $\epsilon_n(z)$ strongly depends on the thickness of the filament. Thinner filament has stronger spacing out of the subbands.

The potential barrier for conducting transmission in the longitudinal direction ($z$) lies in the bottom of the subbands. When the filament is very thick, which means the confinement is weak, the dispersion curve will turn into the 3D bulk energy band. In that case, the bottoms of the subbands are in rather deep energy levels. Whereas, when the filament is very thin, the bottom of the subbands will be lifted. Consequently, the dependence of the energy level of the bottom of the subbands on $z$ in a constricted tube is arch-shaped curves, as shown in Fig. 20c. The number of the subbands is just that of the conducting modes or conducting channels $N_{\mathrm{ch}}$. $\Phi_{\mathrm{B}}$ is the height of the first subband. The barrier width $t_B$ is defined as the width of the first subband at $E = 0$. If the CF is very thick, the barrier disappears. On the contrary, in the HRS state, the CF is

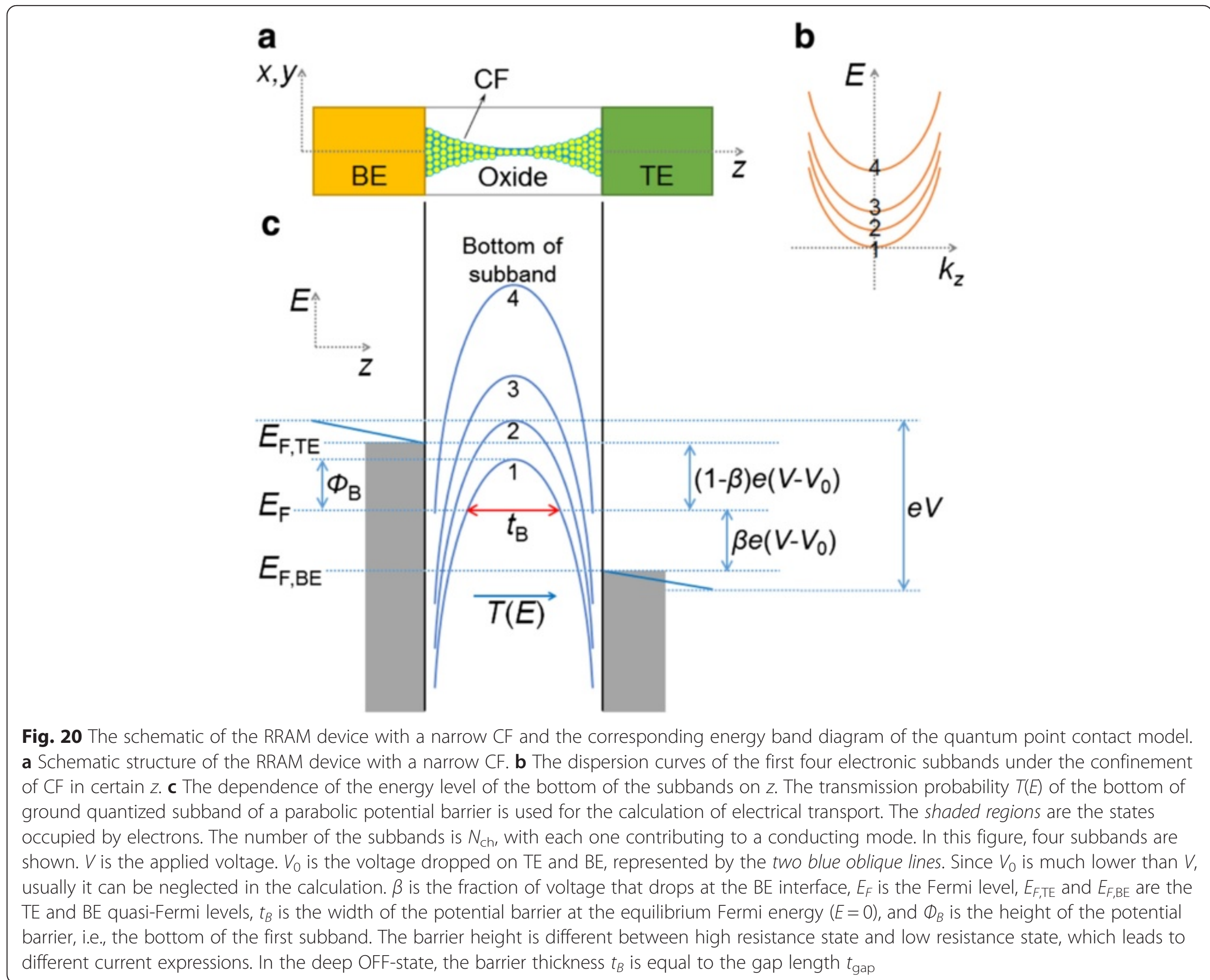


**Fig. 20** The schematic of the RRAM device with a narrow CF and the corresponding energy band diagram of the quantum point contact model. **a** Schematic structure of the RRAM device with a narrow CF. **b** The dispersion curves of the first four electronic subbands under the confinement of CF in certain *z*. **c** The dependence of the energy level of the bottom of the subbands on *z*. The transmission probability *T*(*E*) of the bottom of ground quantized subband of a parabolic potential barrier is used for the calculation of electrical transport. The *shaded regions* are the states occupied by electrons. The number of the subbands is $N_{ch}$, with each one contributing to a conducting mode. In this figure, four subbands are shown. *V* is the applied voltage. $V_0$ is the voltage dropped on TE and BE, represented by the *two blue oblique lines*. Since $V_0$ is much lower than *V*, usually it can be neglected in the calculation. *β* is the fraction of voltage that drops at the BE interface, $E_F$ is the Fermi level, $E_{F,TE}$ and $E_{F,BE}$ are the TE and BE quasi-Fermi levels, $t_B$ is the width of the potential barrier at the equilibrium Fermi energy ($E = 0$), and $\Phi_B$ is the height of the potential barrier, i.e., the bottom of the first subband. The barrier height is different between high resistance state and low resistance state, which leads to different current expressions. In the deep OFF-state, the barrier thickness $t_B$ is equal to the gap length $t_{gap}$

ruptured and there is a gap in the CF region, so the barrier becomes very high. In the conduction, the injected electrons need to travel through the potential barrier, with a transmission probability *T*(*E*).

In QPC model, based on the Landauer theory, the current flowing through the RRAM device can be calculated as [11]

$$I = \frac{2e}{h} N_{\rm ch} \int_{-\infty}^{\infty} T(E)[f(E-\beta eV) - f(E + (1-\beta)eV)]dE, \tag{3}$$

where $E$ is the energy, $f$ is the Fermi-Dirac distribution function, and $N_{ch}$ is the total number of 1D opened conducting channels connecting the electrodes. An inverted parabolic potential barrier is assumed to get an analytical expression for the transmission probability [71]:

$$T(E) = \{1 + \exp[-\alpha_B(E-\Phi_B)]\}^{-1}, \tag{4}$$

where $\alpha_B$ is related to the inverse of potential barrier curvature and is proportional to the thickness of the barrier, i.e., $\alpha_B = t_B \pi^2 h^{-1} \sqrt{2m^*/\Phi_B}$ [71, 214]. $m^*$ is the effective electron mass. Inserting Eq. (4) into Eq. (3), we can get

$$I \approx \frac{2e}{h} N_{\rm ch} \left\{ eV + \frac{1}{\alpha} {\rm Ln} \left[ \frac{1 + \exp\{\alpha_B[\Phi_B - \beta eV]\}}{1 + \exp\{\alpha_B[\Phi_B + (1-\beta eV)eV]\}} \right] \right\} \tag{5}$$

Equation (5) is applicable for both HRS and LRS, with the difference in the values of $\alpha_B$ and $\Phi_B$ which represent the difference in potential barrier. In HRS, there is a gap in the CF region, so at low applied voltages (i.e., $V \to 0$), Eq. (5) can be simplified as

$$I \cong N_{\rm ch} G_0 \exp(-\alpha_B \Phi_B) V. \tag{6}$$

So, the conduction in HRS is just determined by the barrier through the parameters $\alpha_B$ and $\Phi_B$ [215, 216, 219]. While in LRS, there is no spatial gap, so Eq. (5) converges to

$$I \cong N_{ch}\beta G_0 V, \tag{7}$$

which is a linear $I$–$V$, consistent with that usually observed in LRS. When the CF is very narrow, i.e., when $N_{ch}$ is small, Eq. (7) accounts well for the experimentally observed conductance quantization effects. The CF conductance is expressed as

$$G \cong N_{ch}\beta G_0, \tag{8}$$

showing that $G$ is just the integer multiples of the quantum of conductance $G_0$, when the voltage drop at two interfaces is asymmetric, i.e., $\beta = 1$. If $N_{ch}$ is large, the model approaches the classical Ohmic regime, where quantization effect is less evident since CF conductance is high.

It is worth noting that there are some amounts of experimental points whose conductance is smaller than $G_0$, according to the reported results as shown in "Conductance Quantization in RRAM" and "Structures, Materials, and Operation Methods of RRAM with QC Effect" section. Values slightly different from $G_0$ are possible even when a continuous conducting channel connects the electrodes, since in Eq. (8), $N_{ch}$ is an integer whereas $0 < \beta < 1$. In an atomic-scale conducting CF or quantum wire (QW), the voltage mainly drops at the interfaces with the external reservoirs and the value of $\beta$ is the fraction of voltage that drops at the BE interface. The value of $\beta$ might change with the actual geometry of the CF and with its coupling to the reservoirs. The presence of impurities in the QW or non-adiabatic coupling with the reservoirs might also explain a conductance smaller than $G_0$ for each conducting mode [153]. The adsorbed impurities on or in atom chains would change the CF constriction configuration and influence the electronic band structure.

In a subsequent work, Miranda et al. proposed a simple current–voltage model based on the quantized constriction of RRAM (Fig. 21) and explained the minimum unit of conductance of 0.5 $G_0$. The left-going current $I^-$ and right-going current $I^+$ were respectively calculated as:

$$I^+ = \frac{2e}{h}\int_{-\infty}^{\infty} T(E)M(E)f(E - \beta eV)dE \tag{9}$$

and

$$I^- = \frac{2e}{h}\int_{-\infty}^{+\infty} T(E)M(E)f[E + (1-\beta)eV]dE, \tag{10}$$

where $M$ represents the number of conduction modes, and the voltage dropped in electrodes $V_0$ is neglected. The total current $I = I^+ - I^-$ is given as:

$$I = G_0[\beta N^+ + (1-\beta)N^-]V, \tag{11}$$

where $N^+$ and $N^-$ are the number of right-going and left-going conduction modes, respectively, i.e., the number of subbands with $E \leq \beta e(V - V_0)$ and $E \leq -(1 - \beta)e(V - V_0)$ in Fig. 21, respectively. For simplicity, considering the case of

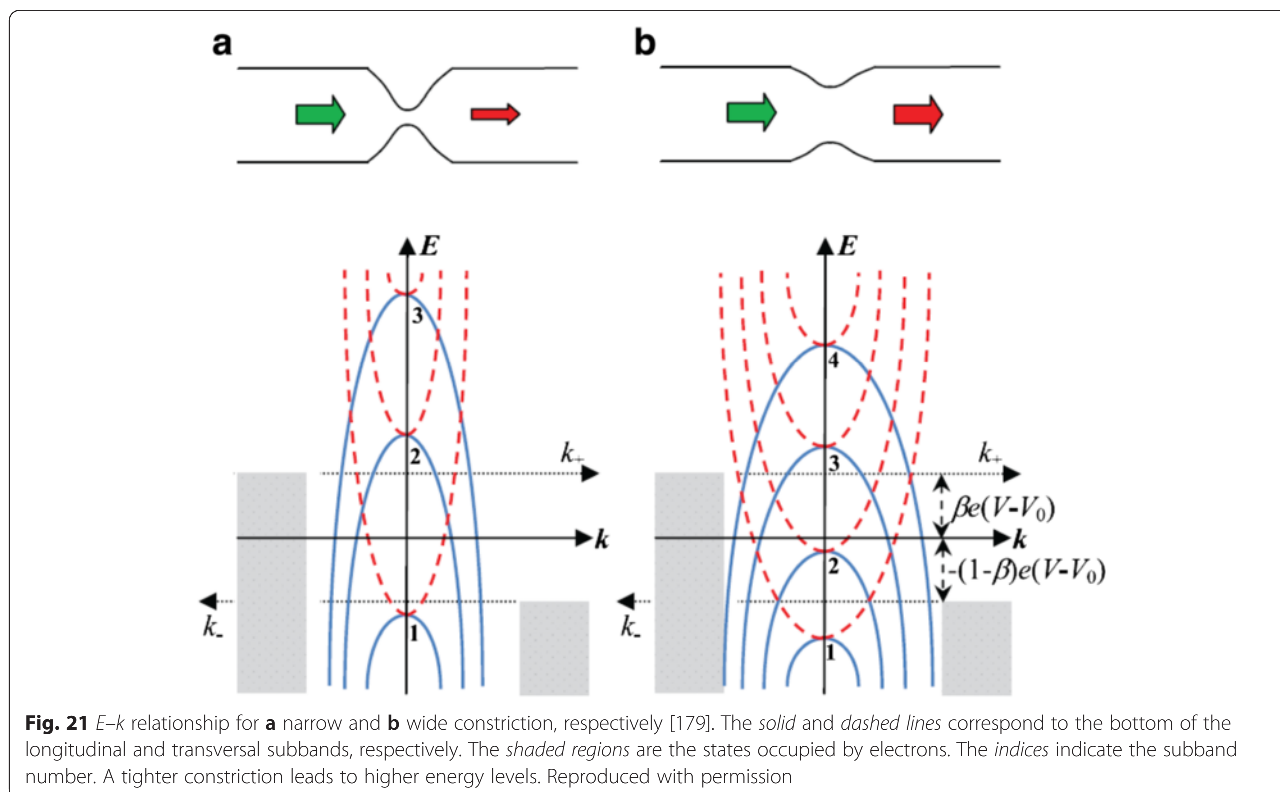


**Fig. 21** *E–k* relationship for **a** narrow and **b** wide constriction, respectively [179]. The *solid* and *dashed lines* correspond to the bottom of the longitudinal and transversal subbands, respectively. The *shaded regions* are the states occupied by electrons. The *indices* indicate the subband number. A tighter constriction leads to higher energy levels. Reproduced with permission

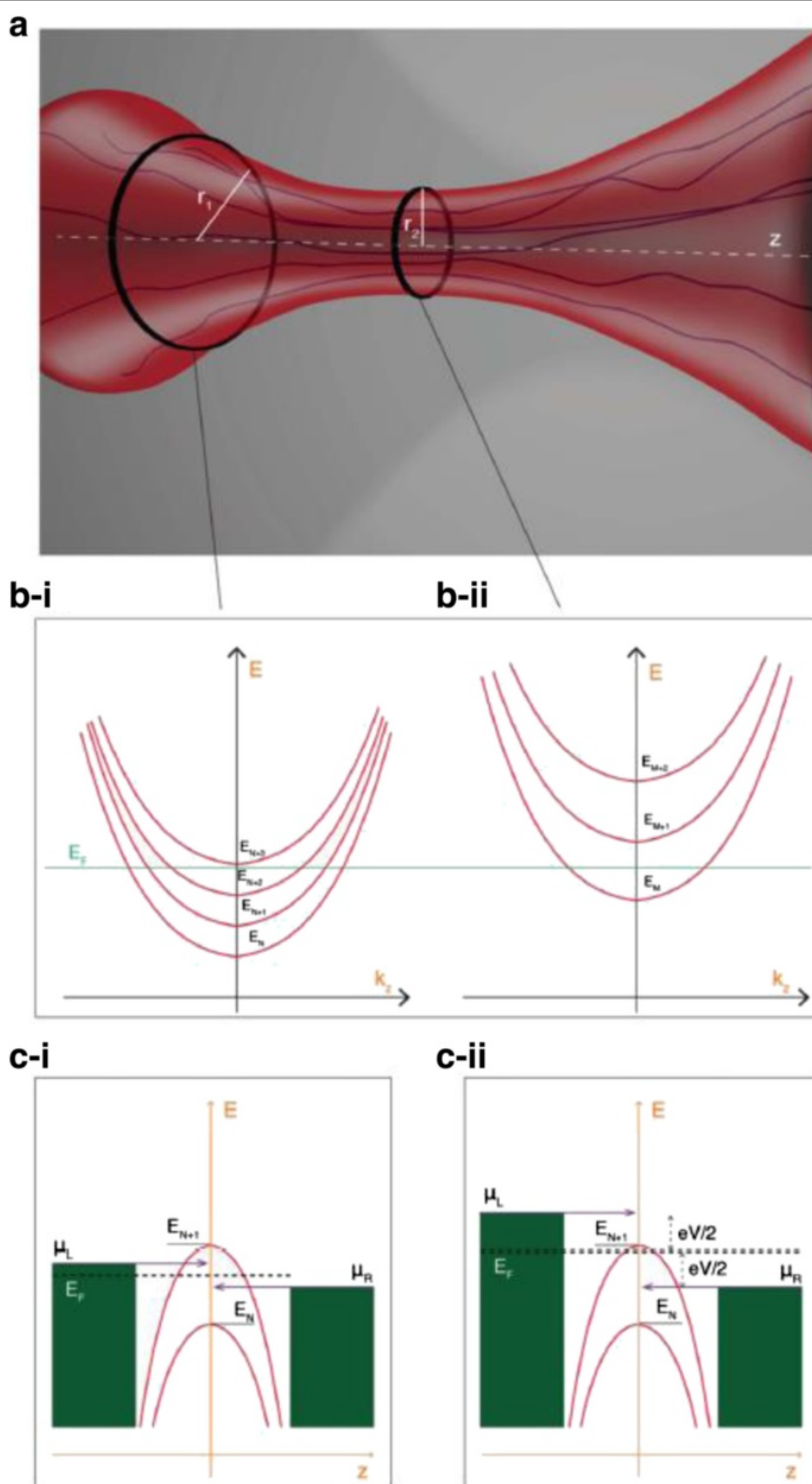


**Fig. 22** (See legend on next page.)

(See figure on previous page.)
**Fig. 22** Quantized conductance effect based on the quantum point contact model [186]. **a** Schematic illustration of a conducting filament with a lateral constriction of one or several atoms at the narrowest part of the filament. **b-I** Dispersion curves of the first four electronic subbands at the edge of the constriction. **b-II** Dispersion curves of the first three subbands at the center of the constriction where the confinement is stronger which leads to a spacing out of the subbands. **c-I** When the difference in chemical potential between the left and right reservoirs is small, both the left-going and right-going electron modes fall within the same subband. **c-II** When the difference in chemical potential between the two reservoirs is large, the left-going and right-going electron modes fall into different subbands. Reproduced with permission

a symmetric potential drop at two ends of the constriction, $\beta$ equals 0.5, thus Eq. (11) indicates that when the difference of $N^{+} + N^{-}$ is an odd number, the conductance values of half-integer multiples of $G_0$ appear. Simulation results fit well with the experimental results measured in $W/CeO_x/SiO_2/NiSi_2$ devices [179].

A similar model was proposed by Mehonic et al. [186]. This model treats filaments as quantum constrictions within the framework of Landauer theory. In this model, the potential drop on the two ends of the constriction is not assumed to be symmetric.

The schematic illustration of this model is shown in Fig. 22. The lateral confined quantum constriction for carriers to flow through produces a set of discrete one-dimensional subbands in the conduction band. More conduction modes are allowed if the size of the constriction increases. Half-integer quantum conductance was studied under the quantum point conduction model. By assuming the transmission probability to be one for electrons with energy above the minimum energy value of the subband, to be zero with energy below this, and adopting the zero temperature limit, the total current is

$$I = I_R - I_L = \frac{1}{2}(N_R + N_L)G_0 V, \qquad (12)$$

where $N_R$ and $N_L$ are the numbers of occupied subbands accessed from the right and left sides, respectively. Here, symmetric voltage drop in the TE and BE interfaces is assumed, i.e., $\beta = 0.5$. Then, the half-integer quantum value appears when $N_R + N_L$ is an odd number, which is in coherence with the result reported by Miranda et al. as described above. In all ECM devices, since the electron reservoirs are highly conductive, it is impossible to maintain a large difference in chemical potential, which is the reason for the difficult observation of half-integer quantization. While in another case, i.e., in VCM devices, most of them exhibit half-integer quantization. An important conclusion drawn in this paper is that the key quantity governing the type of quantization is the difference in chemical potentials between the two reservoirs.

The appearance of half-integer multiples of quantized conductance might also arise from the absence of the spin degeneracy. The quantum of conductance $G_0$, i.e., $2e^2/h$, is equally contributed by two spin-degenerate transport channels. Thus, in nonmagnetic materials where the spin degeneracy is reserved, the conductance is the integral multiple of $G_0$. While when the spin degeneracy is broken in magnetic systems, a single spin channel will contribute a conductance of 0.5 $G_0$, i.e., $e^2/h$, leading to the conductance of half-integral multiple of $G_0$. As easily inferred from Table 2, the half-integer $G_0$ appears mostly when the CF is composed of Vo. That is because the Vo can carry a weak magnetism in some cases, according to lots of previous studies [41, 220]. The magnetic CF may bring spin-splitting conductance channels, which give rise to the observed 0.5 $G_0$.

#### *First Principle Calculation on the Quantized Conductance of Oxygen Vacancy Conductive Filament*

As mentioned above, before switching to the high resistance state, the CF in RRAM behaves as a nanoscale conductive path with a few defects such as oxygen vacancies. It is necessary to explore whether the oxygen vacancy paths can explain the quantized conductance behavior. First principle calculations based on the density-functional theory (DFT) were carried out to get the quantized conductance of oxygen vacancy conductive path in crystalline $HfO_2$ matrix [69]. In this work, the zero-bias transmission probability $T(E)$ was calculated by using non-equilibrium Green's functions. The ballistic conductance was calculated through first principle method based on Landauer theory. The conductance of CF was then calculated via the Landauer formula, $G = T(E)G_0$. The generation of an oxygen vacancy is considered as the removal of an oxygen atom in a monoclinic-$HfO_2$ host. As a result, a filled impurity state is introduced in the band gap which is far from the band edges, as shown in Fig. 23a. The spatial spread of the impurity wavefunction determines that the states overlap between two neighboring oxygen vacancies, which further determines whether the carrier transport is hopping or band transport. As shown by the band structures of monoclinic-$HfO_2$ with a chain of oxygen vacancies in Fig. 23a–d, when oxygen vacancies are closer together, the overlap between the impurity wavefunctions increases, thus the impurity band width also increases. Therefore, the transition from hopping to band transport will occur, with a critical oxygen vacancy concentration of about $1.5 \times 10^{21}$ $cm^{-3}$ corresponding to a local composition $HfO_{2-x}$ with $x = 0.05$. Figure 23e shows the effect of atomic-sized changes in the

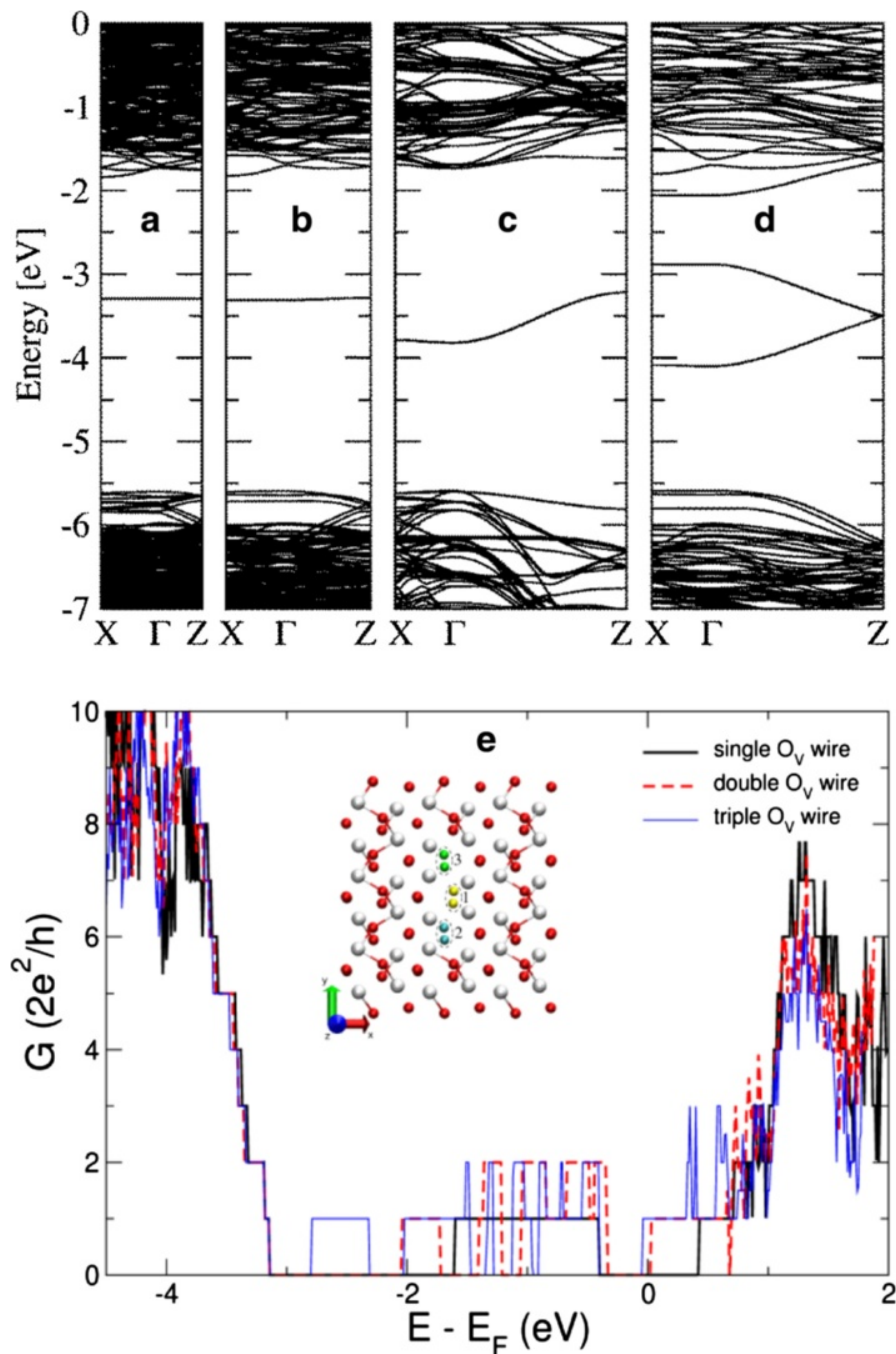


**Fig. 23** Calculated band structures for crystalline m-$HfO_2$ with O vacancies and the corresponding conductance [69]. **a**–**d** Crystalline m-$HfO_2$ band structure with different oxygen vacancies separated by 4 $a_0$, 2 $a_0$, $a_0$, and $a_0$/2. $a_0$ is the length of the c-axis vector for the m-$HfO_2$ primitive cell (0.5296 nm). **e** Conductance as a function of energy corresponding to a $HfO_2$ matrix where one, two, or three O atom rows are removed. The rows subsequently removed are shown in the instate (marked as "1," "2," and "3"), where *red* and *white spheres* correspond to O and Hf atoms, respectively. Reproduced with permission

CF diameter on the obvious change of the CF conductance. When one to three oxygen vacancy columns are formed, as shown by the inset of Fig. 23e, the conductance is observed to increase stepwise, with each transmitting channel contributing a quantum of conductance $G_0$. This result is in qualitative agreement with the interpretation that the filament with single- to few atom diameters behaves as a quantum wire and the observed conductance

quantization originates from single or few atom changes in the atomic structure of the filament.

### *Equivalent Circuit Model for ECM Device Showing Conductance Quantization Effect*

Valov and Waser et al. have found that the ECM device is inherently controlled by the non-equilibrium states, which are induced by several factors, including the chemical processes such as the dissolution of the active electrode materials into the electrolyte, the electrochemical processes, and the charge redistribution during operations [221]. The most distinct effect brought out by the non-equilibrium states is the generation of the electromotive force (emf) in the device, suggesting the presence of a nanobattery inside the device. On the basis of this work, recently they proposed a circuit model (Fig. 24a) for the ECM device accounting for quantized conductance [195, 213]. The discharging of the internal emf voltage ($V_{\mathrm{emf}}$) can influence the device characteristics including ON-resistance ($R_{\mathrm{ON}}$). In the model, they assumed that in the ON-state with atom point contact, the ON-resistance is restricted in the contact regime, being $R_{\mathrm{ON}} = R_{\mathrm{c}} = nG_0^{-1}$, and assumed that $R_{\mathrm{ON}}$ is directly dependent on the internal emf voltage (($V_{\mathrm{emf}}$)). Figure 24b shows the simulation results about the impact of the external resistance $R_{\mathrm{ext}}$ on $R_{\mathrm{ON}}$, exhibiting the staircase-like change of the cell conductance, which well accounts for the experimental results as shown in Fig. 24c. Moreover, the calculated time constants also fit the experimental data as shown in Fig. 24c quite well.

## Prospects of Conductance Quantization in Applications

In these years, the conductance quantization phenomenon in RRAM has been widely investigated and developed, turning into an attractive and well-known effect. From the reported results on the conductance quantization in RRAM, the filament can be of atomic dimensions at the narrowest constriction, which shows that CF-type RRAM devices can still remain functional even if the diameter of CF scales down to the atomic size. Therefore, the ultimate scalability of RRAM is significantly higher than any current mainstream and emerging non-volatile memory.

As many reports have pointed out, one of the potential applications of conductance quantization effect is in multi-level ultra-high-density storage [8, 170]. According to the results in “Structures, Materials, and Operation Methods of RRAM with QC Effect” section, by carefully controlling the resistive switching process of RRAM device, for example, through accurately choosing appropriate compliance current, stop voltage, sweeping speed, pulse conditions, etc., the quantized conductance values can be well controlled in theory, thus multi-level storage can be realized. Since the controllability of quantized states of CF has been confirmed to gradually improve year after year, and at the same time the kinetics and physics of switching processes and conductance quantization have also been revealed to be much clearer [16, 222], the prospect of realizing ultra-high data storage by taking advantage of the phenomenon of conductance quantization has become more promising nowadays. Except the multi-level storage, basic logic circuits can also be realized. The best achievement is from the group of Prof. M. Aono [169]. Low-power logic gates such as AND, OR, NOT gate have been configured making use of quantized conductance atomic switches (QCASs), which were fabricated by crossing metal electrode wires with solid electrolyte wires. However, in order to advance the practical multi-level high-density storage or logic circuit application

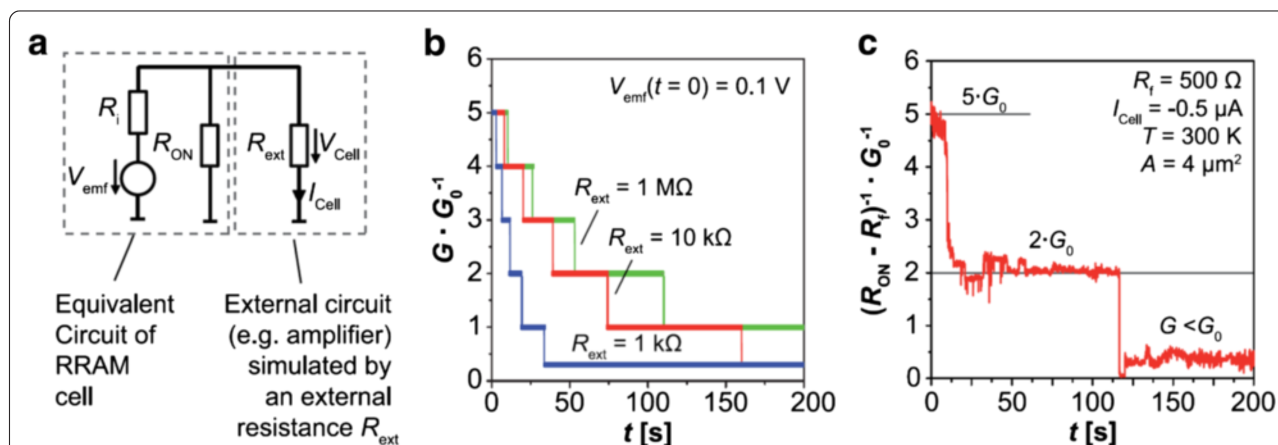


**Fig. 24** Equivalent circuit model for ECM device [195]. **a** Equivalent circuit model for an ECM cell including a nanobattery $V_{\mathrm{emf}}$ with an external circuit. $R_{\mathrm{i}}$ is the total resistance of the ionic current path. $R_{\mathrm{ext}}$ is the external resistance, e.g., from the neighboring cells in an array or a sense amplifier. **b** SPICE simulation results showing a staircase-like change of the cell conductance resulted from the discharging of $V_{\mathrm{emf}}$. **c** Evolution of the conductance of a Ag/$SiO_2$/Pt cell in crossbar structure under a negative cell current $I_{\mathrm{cell}}$. Reproduced with permission

of conductance quantization in RRAM, in the future, deeper investigations should be focused on how to achieve the accurate control of the quantized conductance states, and great improvements should also be required in the multi-level storage performances including endurance, retention, etc., especially based on the pulse operations.

Another important aspect related to the conductance quantization effect in RRAM devices is that the quantized CF can be made use of to investigate any other novel physical effects, such as magnetic and thermoelectric properties. Some works on the magnetic modulation in RRAM have been reported [30–42, 44–46], most of which just studied the RRAM devices with usual oxygen vacancies of CF or metal CF. Our group has also investigated the intrinsic electron transport mechanism in the formed CF by measuring the thermoelectric Seebeck effect [223]. The small-polaron hopping model can well account for the electronic transport process for all resistance states of $Ti/HfO_2/Pt$ device, although the corresponding resistance-temperature behaviors are contradictive. At the same time, from the point of view of device design, the controlled atomic-scale CF in simple two-terminal devices usually got at room temperature and in air can provide a media or platform to develop new one-dimensional nanodevices based on the quantum effects in CF. Here, we just show an interesting example. By replacing the electrode material with magnetic metals, we can configure the magnetic CF, and through electrical manipulation, we can try to control the CF size to get atom-sized magnetic CF. Thus, the magnetic properties such as the quantized anisotropic magnetoresistance (QAMR) effect can be studied in the atom-sized magnetic CF so as to deeply investigate the quantized transport of CF. This kind of works can provide a new characterization method for the research on the CF and the resistive switching mechanism. They might also provide a new idea of achieving stable QAMR effect in experiments and promote the deep understanding on the spin-dependent transport properties in atom-sized materials. In the long term, by simultaneously manipulating the resistance states and the ordered/disordered magnetic states, we might construct novel functional nanoscale electronic devices.

## Conclusions

In this paper, we explained the resistive switching mechanism and operating principles of filamentary RRAM and analyzed their connection with the conductance quantization effect. Then, we introduced some typical researches on the conductance quantization effect of RRAM. The device structures, switching material system, and the operating methods of RRAM related to conductance quantization effect were summarized in detail. Next, the theory and modeling of quantum transport in the atomic CF of RRAM ascribing to the conductance quantization effect were discussed. Finally, we evaluated the opportunities and challenges of the quantized CF system in RRAM devices for the multi-level storage and any other applications in the future.

#### Abbreviations

2DEG: Two-dimensional electron gas; AFM: Atomic force microscopy; BD: Breakdown; CAFM: Conductive atomic force microscopy; CBRAM: Conductive bridge random access memory; CeRAM: Correlated random access memory; CF: Conductive filament; COMS: Complementary metal-oxide-semiconductor; DFT: Density-functional theory; ECM: Electrochemical metallization; emf: Electromotive force; FET: Field effect transistor; HRS: High resistance state; HRTEM: High-resolution transmission electron microscopy; IMT: Insulator-metal transition; IRS: Initial resistance state; LRS: Low resistance state; MIM: Metal-insulator-metal; MRAM: Magnetic random access memory; NVM: Non-volatile memory; PMC: Programmable metallization cell; PRAM: Phase change random access memory; QAMR: Quantized anisotropic magnetoresistance; QC: Quantized conductance; QCAS: Quantized conductance atomic switch; QPC: Quantum point contact; QW: Quantum wire; RRAM: Resistive random access memory; RS: Resistive switching; STEM: Scanning transmission electron microscopy; STM: Scanning tunneling microscope; TCM: Thermochemical mechanism; VCM: Valence change memory; Vo: Oxygen vacancy.

#### Competing interests

The authors declare that they have no competing interests.

#### Authors' contributions

Y Li reviewed the literatures under the instruction of SL. Y Li and SL drafted and revised the manuscript. Y Liu, CH, and JT contributed to the discussion of the quantum transport. QL, HL, JS, and ML suggested many helpful issues for improving the review paper. JS and ML revised the paper thoroughly. All authors read and approved the final manuscript.

#### Acknowledgements

This work was supported by the National Natural Science Foundation of China under Grant Nos. 61322408, 61221004, 61574169, 61274091,61522048, 61422407, 61334007, and 61474135, Beijing Training Project for the Leading Talents in S & T under Grant No. ljrc201508, the National High Technology Research Development Program under Grant No. 2014AA032900, the Opening Project of Key Laboratory of Microelectronics Devices and Integrated Technology, Institute of Microelectronics, Chinese Academy of Sciences, the Spanish Ministry of Science and Technology under contract TEC2012-32305 (partially funded by the EU FEDER program), and the DURSI of the Generalitat de Catalunya under contract 2014SGR384.

#### Author details

[1]Key Laboratory of Microelectronics Devices and Integrated Technology, Institute of Microelectronics, Chinese Academy of Sciences, Beijing 100029, China. [2]Lab of Nanofabrication and Novel Device Integration, Institute of Microelectronics, Chinese Academy of Sciences, Beijing 100029, China. [3]Department of Materials Physics and Chemistry, University of Science and Technology Beijing, Beijing 100083, China. [4]Departament d'Enginyeria Electrònica, Universitat Autònoma de Barcelona, Bellaterra 08193, Spain.

Received: 13 August 2015 Accepted: 12 October 2015
Published online: 26 October 2015

#### References

1. Pirovano A, Schuegraf K (2010) Memory grows up. Nature Nanotech 5(3):177–8. doi:10.1038/nnano.2010.36
2. Fujisaki Y (2013) Review of emerging new solid-state non-volatile memories. Jpn J Appl Phys 52(4R):040001. doi:10.7567/jjap.52.040001
3. Waser R, Aono M (2007) Nanoionics-based resistive switching memories. Nature Mater 6(11):833–40
4. Sawa A (2008) Resistive switching in transition metal oxides. Mater Today 11(6):28–36. doi:10.1016/s1369-7021(08)70119-6
5. Waser R, Dittmann R, Staikov G, Szot K (2009) Redox-based resistive switching memories—nanoionic mechanisms, prospects, and challenges. Adv Mater 21(25–26):2632–63. doi:10.1002/adma.200900375

6. Yang JJ, Strukov DB, Stewart DR (2013) Memristive devices for computing. Nature Nanotech 8(1):13–24. doi:10.1038/nnano.2012.240
7. Jeong DS, Thomas R, Katiyar RS, Scott JF, Kohlstedt H, Petraru A et al (2012) Emerging memories: resistive switching mechanisms and current status. Rep Prog Phys 75(7):076502. doi:10.1088/0034-4885/75/7/076502
8. Pan F, Gao S, Chen C, Song C, Zeng F (2014) Recent progress in resistive random access memories: materials, switching mechanisms, and performance. Mater Sci Eng R-Rep 83:1–59. doi:10.1016/j.mser.2014.06.002
9. Pan F, Chen C, Wang Z-S, Yang Y-C, Yang J, Zeng F (2010) Nonvolatile resistive switching memories—characteristics, mechanisms and challenges. Progress in Natural Science: Materials International 20:1–15. doi:10.1016/s1002-0071(12)60001-x
10. Burr GW, Kurdi BN, Scott JC, Lam CH, Gopalakrishnan K, Shenoy RS (2008) Overview of candidate device technologies for storage-class memory. IBM J Res Dev 52(4/5):449–64
11. Akinaga H, Shima H (2010) Resistive random access memory (ReRAM) based on metal oxides. Proc IEEE 98(12):2237–51. doi:10.1109/JPROC.2010.2070830
12. Wong HSP, Heng-Yuan L, Shimeng Y, Yu-Sheng C, Yi W, Pang-Shiu C et al (2012) Metal-oxide RRAM. Proc IEEE 100(6):1951–70. doi:10.1109/JPROC.2012.2190369
13. Karg SF, Meijer GI, Bednorz JG, Rettner CT, Schrott AG, Joseph EA et al (2008) Transition-metal-oxide-based resistance-change memories. IBM J Res Dev 52(4.5):481–92
14. Prakash A, Jana D, Maikap S (2013) $TaO_X$-based resistive switching memories, prospective and challenges. Nanoscale Res Lett 8:418. doi:10.1186/1556-276X-8-418
15. Valov I, Waser R, Jameson JR, Kozicki MN (2011) Electrochemical metallization memories—fundamentals, applications, prospects. Nanotechnology 22(28):289502. doi:10.1088/0957-4484/22/28/289502
16. Valov I, Sapezanskaia I, Nayak A, Tsuruoka T, Bredow T, Hasegawa T et al (2012) Atomically controlled electrochemical nucleation at superionic solid electrolyte surfaces. Nature Mater 11(6):530–5. doi:10.1038/nmat3307
17. Ambrogio S, Balatti S, Choi S, Ielmini D (2014) Impact of the mechanical stress on switching characteristics of electrochemical resistive memory. Adv Mater 26(23):3885–92. doi:10.1002/adma.201306250
18. Tian X, Yang S, Zeng M, Wang L, Wei J, Xu Z et al (2014) Bipolar electrochemical mechanism for mass transfer in nanoionic resistive memories. Adv Mater 26(22):3649–54. doi:10.1002/adma.201400127
19. Valov I (2014) Redox-based resistive switching memories (ReRAMs): electrochemical systems at the atomic scale. Chem Electro Chem 1(1):26–36. doi:10.1002/celc.201300165
20. Yang Y, Gao P, Li L, Pan X, Tappertzhofen S, Choi S et al (2014) Electrochemical dynamics of nanoscale metallic inclusions in dielectrics. Nat Commun 5:4232. doi:10.1038/ncomms5232
21. Russo U, Ielmini D, Cagli C, Lacaita AL, Spiga S, Wiemer C et al (2007) Conductive-filament switching analysis and self-accelerated thermal dissolution model for reset in NiO-based RRAM. IEEE International Electron Devices Meeting (IEDM)
22. Russo U, Ielmini D, Cagli C, Lacaita AL (2009) Self-accelerated thermal dissolution model for reset programming in unipolar resistive-switching memory (RRAM) devices. IEEE Trans Electron Devices 56(2):193–200. doi:10.1109/TED.2008.2010584
23. Seungjae J, Siddik M, Wootae L, Jubong P, Xinjun L, Jiyong W et al (2011) Thermally-assisted $Ti/Pr_{0.7}Ca_{0.3}MnO_3$ ReRAM with excellent switching speed and retention characteristics. IEEE International Electron Devices Meeting (IEDM)
24. Kim S, Kim SJ, Kim KM, Lee SR, Chang M, Cho E et al (2013) Physical electro-thermal model of resistive switching in bi-layered resistance-change memory. Sci Rep 3:1680. doi:10.1038/srep01680
25. Peng S, Zhuge F, Chen X, Zhu X, Hu B, Pan L et al (2012) Mechanism for resistive switching in an oxide-based electrochemical metallization memory. Appl Phys Lett 100(7):072101. doi:10.1063/1.3683523
26. Shang J, Liu G, Yang H, Zhu X, Chen X, Tan H et al (2014) Thermally stable transparent resistive random access memory based on all-oxide heterostructures. Adv Funct Mater 24(15):2171–9. doi:10.1002/adfm.201303274
27. Pan L, Ji Z, Yi X, Zhu X, Chen X, Shang J et al (2015) Metal-organic framework nanofilm for mechanically flexible information storage applications. Adv Funct Mater 25(18):2677–85. doi:10.1002/adfm.201500449
28. Lee HS, Choi SG, Park H-H, Rozenberg MJ. A new route to the Mott-Hubbard metal-insulator transition: Strong correlations effects in $Pr_{0.7}Ca_{0.3}MnO_3$. Sci Rep. 2013; 3. doi:10.1038/srep01704.
29. Mottaghizadeh A, Yu Q, Lang PL, Zimmers A, Aubin H. Metal oxide resistive switching: evolution of the density of states across the metal-insulator transition. Phys Rev Lett. 2014; 112(6). doi:10.1103/PhysRevLett.112.066803.
30. Sokolov A, Sabirianov R, Sabirianov I, Doudin B (2009) Voltage-induced switching with magnetoresistance signature in magnetic nano-filaments. J Phys Condens Matter 21(48):485303. doi:10.1088/0953-8984/21/48/485303
31. Teixeira JM, Ventura J, Fermento R, Araujo JP, Sousa JB, Wisniowski P et al (2009) Electroforming, magnetic and resistive switching in MgO-based tunnel junctions. J Phys D Appl Phys 42(10):105407. doi:10.1088/0022-3727/42/10/105407
32. Pertsev NA, Kohlstedt H (2010) Resistive switching via the converse magnetoelectric effect in ferromagnetic multilayers on ferroelectric substrates. Nanotechnology 21(47):475202. doi:10.1088/0957-4484/21/47/475202
33. Son JY, Kim CH, Cho JH, Shin Y-H, Jang HM (2010) Self-formed exchange bias of switchable conducting filaments in NiO resistive random access memory capacitors. ACS Nano 4(6):3288–92. doi:10.1021/nn100323x
34. Chen G, Song C, Chen C, Gao S, Zeng F, Pan F (2012) Resistive switching and magnetic modulation in cobalt-doped ZnO. Adv Mater 24(26):3515–20. doi:10.1002/adma.201201595
35. Rubi D, Marlasca FG, Reinoso M, Bonville P, Levy P (2012) Magnetism and electrode dependant resistive switching in Ca-doped ceramic bismuth ferrite. Mater Sci Eng B 177(6):471–5. doi:10.1016/j.mseb.2012.02.022
36. Thakare V, Xing G, Peng H, Rana A, Game O, Anil Kumar P et al (2012) High sensitivity low field magnetically gated resistive switching in $CoFe_2O_4/La_{0.66}Sr_{0.34}MnO_3$ heterostructure. Appl Phys Lett 100(17):172412. doi:10.1063/1.4707373
37. Chen G, Peng JJ, Song C, Zeng F, Pan F (2013) Interplay between chemical state, electric properties, and ferromagnetism in Fe-doped ZnO films. J Appl Phys 113(10):104503. doi:10.1063/1.4794882
38. Wang XL, Ku PS, Shao Q, Cheng WF, Leung CW, Ruotolo A (2013) Magnetism as a probe of the origin of memristive switching in p-type antiferromagnetic NiO. Appl Phys Lett 103(22):223508. doi:10.1063/1.4834795
39. Li Q, Shen TT, Cao YL, Zhang K, Yan SS, Tian YF et al (2014) Spin memristive magnetic tunnel junctions with CoO-ZnO nano composite barrier. Sci Rep 4:3835. doi:10.1038/srep03835
40. Otsuka S, Hamada Y, Shimizu T, Shingubara S (2014) Ferromagnetic nano-conductive filament formed in $Ni/TiO_2/Pt$ resistive-switching memory. Appl Phys A 118(2):613–9. doi:10.1007/s00339-014-8769-5
41. Ren SX, Sun GW, Zhao J, Dong JY, Wei Y, Ma ZC et al (2014) Electric field-induced magnetic switching in Mn:ZnO film. Appl Phys Lett 104(23):232406, http://dx.doi.org/10.1063/1.4883259
42. Wang J, Zhang X, Piao H-G, Luo Z, Xiong C, Wang X et al (2014) Magnetic field controllable nonvolatile resistive switching effect in silicon device. Appl Phys Lett 104(24):243511. doi:10.1063/1.4884771
43. Xiong YQ, Zhou WP, Li Q, He MC, Du J, Cao QQ et al (2014) Electric field manipulation of nonvolatile magnetization in Au/NiO/Pt heterostructure with resistive switching effect. Appl Phys Lett 105(3):032410. doi:10.1063/1.4891482
44. Xu Z, Gao M, Yu L, Lu L, Xu X, Jiang Y (2014) Co nanoparticles induced resistive switching and magnetism for the electrochemically deposited polypyrrole composite films. ACS Appl Mater Interfaces 6(20):17823–30. doi:10.1021/am5044399
45. Zhang Z, Jiang L (2014) Bias voltage induced resistance switching effect in single-molecule magnets' tunneling junction. Nanotechnology 25(36):365201. doi:10.1088/0957-4484/25/36/365201
46. Chen X, Zhu X, Xiao W, Liu G, Feng YP, Ding J et al (2015) Nanoscale magnetization reversal caused by electric field-induced ion migration and redistribution in cobalt ferrite thin films. ACS Nano 9(4):4210–8. doi:10.1021/acsnano.5b00456
47. Yang Z, Zhan Q, Zhu X, Liu Y, Yang H, Hu B et al (2014) Tunneling magnetoresistance induced by controllable formation of Co filaments in resistive switching Co/ZnO/Fe structures. EPL (Europhysics Letters) 108(5):58004. doi:10.1209/0295-5075/108/58004
48. Guo X, Schindler C, Menzel S, Waser R (2007) Understanding the switching-off mechanism in $Ag^+$ migration based resistively switching model systems. Appl Phys Lett 91(13):133513. doi:10.1063/1.2793686
49. Sakamoto T, Lister K, Banno N, Hasegawa T, Terabe K, Aono M (2007) Electronic transport in $Ta_2O_5$ resistive switch. Appl Phys Lett 91(9):092110, http://dx.doi.org/10.1063/1.2777170

50. Yang YC, Pan F, Liu Q, Liu M, Zeng F (2009) Fully room-temperature-fabricated nonvolatile resistive memory for ultrafast and high-density memory application. Nano Lett 9(4):1636–43. doi:10.1021/nl900006g
51. Kwon DH, Kim KM, Jang JH, Jeon JM, Lee MH, Kim GH et al (2010) Atomic structure of conducting nanofilaments in $TiO_2$ resistive switching memory. Nature Nanotech 5(2):148–53. doi:10.1038/nnano.2009.456
52. Liu Q, Long S, Lv H, Wang W, Niu J, Huo Z et al (2010) Controllable growth of nanoscale conductive filaments in solid-electrolyte-based ReRAM by using a metal nanocrystal covered bottom electrode. ACS Nano 4(10):6162–8. doi:10.1021/nn1017582
53. Xu Z, Bando Y, Wang W, Bai X, Golberg D (2010) Real-time in situ HRTEM-resolved resistance switching of $Ag_2S$ nanoscale ionic conductor. ACS Nano 4(5):2515–22. doi:10.1021/nn100483a
54. Miao F, Strachan JP, Yang JJ, Zhang MX, Goldfarb I, Torrezan AC et al (2011) Anatomy of a nanoscale conduction channel reveals the mechanism of a high-performance memristor. Adv Mater 23(47):5633–40. doi:10.1002/adma.201103379
55. Liu Q, Sun J, Lv H, Long S, Yin K, Wan N et al (2012) Real-time observation on dynamic growth/dissolution of conductive filaments in oxide-electrolyte-based ReRAM. Adv Mater 24(14):1844–9. doi:10.1002/adma.201104104
56. Yang Y, Gao P, Gaba S, Chang T, Pan X, Lu W (2012) Observation of conducting filament growth in nanoscale resistive memories. Nat Commun 3:732. doi:10.1038/ncomms1737
57. Park GS, Kim YB, Park SY, Li XS, Heo S, Lee MJ et al (2013) In situ observation of filamentary conducting channels in an asymmetric $Ta_2O_{5-X}/TaO_{2-X}$ bilayer structure. Nat Commun 4:2382. doi:10.1038/ncomms3382
58. Celano U, Goux L, Belmonte A, Opsomer K, Franquet A, Schulze A et al (2014) Three-dimensional observation of the conductive filament in nanoscaled resistive memory devices. Nano Lett 14(5):2401–6. doi:10.1021/nl500049g
59. Privitera S, Bersuker G, Butcher B, Kalantarian A, Lombardo S, Bongiorno C et al (2013) Microscopy study of the conductive filament in $HfO_2$ resistive switching memory devices. Microelectron Eng 109:75–8, http://dx.doi.org/10.1016/j.mee.2013.03.145
60. Zhu X-J, Shang J, Liu G, Li R-W (2014) Ion transport-related resistive switching in film sandwich structures. Chin Sci Bull 59(20):2363–82. doi:10.1007/s11434-014-0284-8
61. Szot K, Speier W, Bihlmayer G, Waser R (2006) Switching the electrical resistance of individual dislocations in single-crystalline $SrTiO_3$. Nature Mater 5(4):312–20. doi:10.1038/nmat1614
62. Lee MH, Hwang CS (2011) Resistive switching memory: observations with scanning probe microscopy. Nanoscale 3(2):490–502. doi:10.1039/c0nr00580k
63. Lanza M (2014) A review on resistive switching in high-k dielectrics: a nanoscale point of view using conductive atomic force microscope. Materials 7(3):2155–82. doi:10.3390/ma7032155
64. Victor VZ, Roy M, Ralph KC, Gurtej S (2011) Scaling limits of resistive memories. Nanotechnology 22(25):254027
65. Sharvin YV (1965) A possible method for studying Fermi surfaces. Sov Phys JETP 21:655–656
66. Montie EA, Cosman EC, t Hooft GW, van der Mark MB, Beenakker CWJ (1991) Observation of the optical analogue of quantized conductance of a point contact. Nature 350(6319):594–5
67. Krans JM, van Ruitenbeek JM, Fisun VV, Yanson IK, de Jongh LJ (1995) The signature of conductance quantization in metallic point contacts. Nature 375(6534):767–9
68. Ohnishi H, Kondo Y, Takayanagi K (1998) Quantized conductance through individual rows of suspended gold atoms. Nature 395(6704):780–3, http://www.nature.com/nature/journal/v395/n6704/
69. Long S, Lian X, Cagli C, Cartoixà X, Rurali R, Miranda E et al (2013) Quantum-size effects in hafnium-oxide resistive switching. Appl Phys Lett 102(18):183505. doi:10.1063/1.4802265
70. Long S, Perniola L, Cagli C, Buckley J, Lian X, Miranda E et al (2013) Voltage and power-controlled regimes in the progressive unipolar RESET transition of $HfO_2$-based RRAM. Sci Rep 3:2929. doi:10.1038/srep02929
71. Lian X, Cartoixà X, Miranda E, Perniola L, Rurali R, Long S et al (2014) Multi-scale quantum point contact model for filamentary conduction in resistive random access memories devices. J Appl Phys 115(24):244507, http://dx.doi.org/10.1063/1.4885419
72. Zhao X, Xu H, Wang Z, Zhang L, Ma J, Liu Y (2015) Nonvolatile/volatile behaviors and quantized conductance observed in resistive switching memory based on amorphous carbon. Carbon 91:38–44, http://dx.doi.org/10.1016/j.carbon.2015.04.031
73. Long S, Cagli C, Ielmini D, Liu M, Suñé J (2012) Analysis and modeling of resistive switching statistics. J Appl Phys 111(7):074508. doi:10.1063/1.3699369
74. Zhang M, Long S, Wang G, Li Y, Xu X, Liu H et al (2014) An overview of the switching parameter variation of RRAM. Chin Sci Bull 59(36):5324–37. doi:10.1007/s11434-014-0673-z
75. Daughton JM (1992) Magnetoresistive memory technology. Thin Solid Films 216(1):162–8, http://dx.doi.org/10.1016/0040-6090(92)90888-I
76. Gallagher WJ, Parkin SS (2006) Development of the magnetic tunnel junction MRAM at IBM: from first junctions to a 16-Mb MRAM demonstrator chip. IBM J Res Dev 50(1):5–23
77. Kawahara T, Ito K, Takemura R, Ohno H (2012) Spin-transfer torque RAM technology: review and prospect. Microelectron Reliab 52(4):613–27, http://dx.doi.org/10.1016/j.microrel.2011.09.028
78. Khvalkovskiy A, Apalkov D, Watts S, Chepulskii R, Beach R, Ong A et al (2013) Basic principles of STT-MRAM cell operation in memory arrays. J Phys D Appl Phys 46(7):74001–20
79. Yuasa S, Fukushima A, Yakushiji K, Nozaki T, Konoto M, Maehara H et al. Future prospects of MRAM technologies. Proc IEEE-IEDM (Washington, DC, 9–11 December 2013). 2013:3.1.
80. Zalba B (2003) Marín JM, Cabeza LF, Mehling H. Review on thermal energy storage with phase change: materials, heat transfer analysis and applications. Appl Therm Eng 23(3):251–83
81. Farid MM, Khudhair AM, Razack SAK, Al-Hallaj S (2004) A review on phase change energy storage: materials and applications. Energy Convers Manage 45(9):1597–615
82. Sharma A, Tyagi V, Chen C, Buddhi D (2009) Review on thermal energy storage with phase change materials and applications. Renew Sust Energ Rev 13(2):318–45
83. Zilberberg O, Weiss S, Toledo S (2013) Phase-change memory: an architectural perspective. ACM Computing Surveys (CSUR) 45(3):29
84. Oike H, Kagawa F, Ogawa N, Ueda A, Mori H, Kawasaki M et al (2015) Phase-change memory function of correlated electrons in organic conductors. Phys Rev B Condens Matter 91(4):041101
85. Wentai L, Hangbing L, Liu Q, Long S, Wang W, Wang Y et al (2011) Improved resistive switching uniformity in $Cu/HfO_2/Pt$ devices by using current sweeping mode. IEEE Electron Device Lett 32(8):1053–5. doi:10.1109/LED.2011.2157990
86. Hongtao L, Hangbin L, Baohe Y, Xiaoxin X, Ruoyu L, Qi L et al (2014) Uniformity improvement in 1T1R RRAM with gate voltage ramp programming. IEEE Electron Device Lett 35(12):1224–6. doi:10.1109/LED.2014.2364171
87. Wang G, Long S, Zhang M, Li Y, Xu X, Liu H et al (2014) Operation methods of resistive random access memory. Sci China Tech Sci 57(12):2295–304. doi:10.1007/s11431-014-5718-7
88. Waser R (2009) Resistive non-volatile memory devices (Invited Paper). Microelectron Eng 86(7–9):1925–8. doi:10.1016/j.mee.2009.03.132
89. Kim KM, Jeong DS, Hwang CS (2011) Nanofilamentary resistive switching in binary oxide system: a review on the present status and outlook. Nanotechnology 22(25):254002. doi:10.1088/0957-4484/22/25/254002
90. Lu W, Jeong DS, Kozicki M, Waser R (2012) Electrochemical metallization cells—blending nanoionics into nanoelectronics? MRS Bull 37(02):124–30. doi:10.1557/mrs.2012.5
91. Yang JJ, Inoue IH, Mikolajick T, Hwang CS (2012) Metal oxide memories based on thermochemical and valence change mechanisms. MRS Bull 37(02):131–7. doi:10.1557/mrs.2011.356
92. Valov I, Kozicki MN (2013) Cation-based resistance change memory. J Phys D Appl Phys 46(7):074005. doi:10.1088/0022-3727/46/7/074005
93. The international technology roadmap for semiconductors (ITRS), process integration, devices, and structures summary, 2013, http://www.itrs.net/
94. Xue WH, Xiao W, Shang J, Chen XX, Zhu XJ, Pan L et al (2014) Intrinsic and interfacial effect of electrode metals on the resistive switching behaviors of zinc oxide films. Nanotechnology 25(42):425204. doi:10.1088/0957-4484/25/42/425204
95. Tan H, Liu G, Zhu X, Yang H, Chen B, Chen X et al (2015) An optoelectronic resistive switching memory with integrated demodulating and arithmetic functions. Adv Mater 27(17):2797–803. doi:10.1002/adma.201500039

96. Feng P, Shong Y, Subramanian V (2011) A detailed study of the forming stage of an electrochemical resistive switching memory by KMC simulation. IEEE Electron Device Lett 32(7):949–51. doi:10.1109/LED.2011.2143691
97. Wu W, Wang ZL (2011) Piezotronic nanowire-based resistive switches as programmable electromechanical memories. Nano Lett 11(7):2779–85. doi:10.1021/nl201074a
98. Kim Y, Strelcov E, Hwang IR, Choi T, Park BH, Jesse S et al (2013) Correlative multimodal probing of ionically-mediated electromechanical phenomena in simple oxides. Sci Rep 3:2924. doi:10.1038/srep02924
99. Li L (2013) Electromechanically tuned resistive switching device. Appl Phys Lett 103(23):233512. doi:10.1063/1.4839415
100. Menzel S, Waser R (2013) Analytical analysis of the generic SET and RESET characteristics of electrochemical metallization memory cells. Nanoscale 5(22):11003–10. doi:10.1039/c3nr03387b
101. Onofrio N, Guzman D, Strachan A (2015) Atomic origin of ultrafast resistance switching in nanoscale electrometallization cells. Nature Mater 14(4):440–6. doi:10.1038/nmat4221
102. Wei Z, Kanzawa Y, Arita K, Katoh Y, Kawai K, Muraoka S et al (2008) Highly reliable $TaO_X$ ReRAM and direct evidence of redox reaction mechanism. IEEE International Electron Devices Meeting (IEDM)
103. Zhuge F, Dai W, He CL, Wang AY, Liu YW, Li M et al (2010) Nonvolatile resistive switching memory based on amorphous carbon. Appl Phys Lett 96(16):3. doi:10.1063/1.3406121
104. Chang K-C, Tsai T-M, Chang T-C, Syu Y-E, Wang C-C, Chuang S-L et al (2011) Reducing operation current of Ni-doped silicon oxide resistance random access memory by supercritical $CO_2$ fluid treatment. Appl Phys Lett 99(26):263501, http://dx.doi.org/10.1063/1.3671991
105. Di F, Dan X, Tingting F, Zhang C, Niu J, He Q et al (2011) Unipolar resistive switching properties of diamondlike carbon-based RRAM devices. IEEE Electron Device Lett 32(6):803–5. doi:10.1109/LED.2011.2132750
106. Yu S, Guan X, Wong HSP (2011) Conduction mechanism of TiN / $HfO_X$ / Pt resistive switching memory: a trap-assisted-tunneling model. Appl Phys Lett 99(6):063507. doi:10.1063/1.3624472
107. Chang KC, Tsai TM, Chang TC, Wu HH, Chen KH, Chen JH et al (2013) Low temperature improvement method on Zn:$SiO_x$ resistive random access memory devices. IEEE Electron Device Lett 34(4):511–3. doi:10.1109/LED.2013.2248075
108. Kuan-Chang C, Chih-Hung P, Ting-Chang C, Tsung-Ming T, Rui Z, Jen-Chung L et al (2013) Hopping effect of hydrogen-doped silicon oxide insert RRAM by supercritical $CO_2$ fluid treatment. IEEE Electron Device Lett 34(5):617–9. doi:10.1109/LED.2013.2251995
109. Zhang R, Chang K-C, Chang T-C, Tsai T-M, Chen K-H, Lou J-C et al (2013) High performance of graphene oxide-doped silicon oxide-based resistance random access memory. Nanoscale Res Lett 8(1):1–6. doi:10.1186/1556-276X-8-497
110. Chen Y-J, Chen H-L, Young T-F, Chang T-C, Tsai T-M, Chang K-C et al (2014) Hydrogen induced redox mechanism in amorphous carbon resistive random access memory. Nanoscale Res Lett 9(1):1–5. doi:10.1186/1556-276X-9-52
111. Hong DS, Chen YS, Li Y, Yang HW, Wei LL, Shen BG et al (2014) Evolution of conduction channel and its effect on resistance switching for Au-$WO_{3-x}$-Au devices. Sci Rep 4:4058. doi:10.1038/srep04058
112. Wang G, Long S, Yu Z, Zhang M, Ye T, Li Y et al (2015) Improving resistance uniformity and endurance of resistive switching memory by accurately controlling the stress time of pulse program operation. Appl Phys Lett 106(9):092103, http://dx.doi.org/10.1063/1.4907604
113. Raghavan N, Pey KL, Wu X, Wenhu L, Bosman M (2012) Percolative model and thermodynamic analysis of oxygen-ion-mediated resistive switching. IEEE Electron Device Lett 33(5):712–4. doi:10.1109/LED.2012.2187170
114. Wu PM, Paschoal W, Kumar S, Borschel C, Ronning C, Canali CM et al (2012) Thermoelectric characterization of electronic properties of GaMnAs nanowires. J Nanotechnol 2012:1–5. doi:10.1155/2012/480813
115. Otsuka W, Miyata K, Kitagawa M, Tsutsui K, Tsushima T, Yoshihara H et al. A 4 Mb conductive-bridge resistive memory with 2.3GB/s read-throughput and 216 MB/s program-throughput. IEEE International Solid-State Circuits Conference Digest of Technical Papers (ISSCC); 2011 Feb. 20–24.
116. Shimeng Y, Wong HSP (2011) Compact modeling of conducting-bridge random-access memory (CBRAM). IEEE Trans Electron Devices 58(5):1352–60. doi:10.1109/TED.2011.2116120
117. Seol C, Balatti S, Nardi F, Ielmini D (2012) Size-dependent drift of resistance due to surface defect relaxation in conductive-bridge memory. IEEE Electron Device Lett 33(8):1189–91. doi:10.1109/LED.2012.2199074
118. Zhang K-L, Liu K, Wang F, Yin F-H, Wei X-Y, Zhao J-S (2013) Modeling of conducting bridge evolution in bipolar vanadium oxide-based resistive switching memory. Chin Phys B 22(9):097101. doi:10.1088/1674-1056/22/9/097101
119. Belmonte A, Degraeve R, Fantini A, Kim W, Houssa M, Jurczak M et al (2014) Origin of the deep reset and low variability of pulse-programmed W\$Al_2O_3$\TiW\Cu CBRAM device. IEEE International Memory Workshop (IMW)
120. Russo U, Kamalanathan D, Ielmini D, Lacaita AL, Kozicki MN (2009) Study of multilevel programming in programmable metallization cell (PMC) memory. IEEE Trans Electron Devices 56(5):1040–7. doi:10.1109/TED.2009.2016019
121. Shimeng Y, Wong HSP (2010) Modeling the switching dynamics of programmable-metallization-cell (PMC) memory and its application as synapse device for a neuromorphic computation system. IEEE International Electron Devices Meeting (IEDM)
122. Puthentheradam SC, Schroder DK, Kozicki MN (2011) Inherent diode isolation in programmable metallization cell resistive memory elements. Appl Phys A 102(4):817–26. doi:10.1007/s00339-011-6292-5
123. Wang Z, Kadohira T, Tada T, Watanabe S (2007) Nonequilibrium quantum transport properties of a silver atomic switch. Nano Lett 7(9):2688–92. doi:10.1021/nl0711054
124. Wang Z, Gu T, Tada T, Watanabe S (2008) Excess-silver-induced bridge formation in a silver sulfide atomic switch. Appl Phys Lett 93(15):152106. doi:10.1063/1.2963197
125. Cario L, Vaju C, Corraze B, Guiot V, Janod E (2010) Electric-field-induced resistive switching in a family of mott insulators: Towards a new class of RRAM memories. Adv Mater 22(45):5193–7. doi:10.1002/adma.201002521
126. Celinska J, McWilliams C, Paz de Araujo C, Xue K-H (2011) Material and process optimization of correlated electron random access memories. J Appl Phys 109(9):091603, http://dx.doi.org/10.1063/1.3581197
127. McWilliams CR, Celinska J, de Araujo CA P, Xue K-H (2011) Device characterization of correlated electron random access memories. J Appl Phys 109(9):091608, http://dx.doi.org/10.1063/1.3581206
128. Kim H-T, Chae B-G, Youn D-H, Kim G, Kang K-Y, Lee S-J et al (2005) Raman study of electric-field-induced first-order metal-insulator transition in $VO_2$-based devices. Appl Phys Lett 86(24):242101–3
129. Ruzmetov D, Gopalakrishnan G, Deng J, Narayanamurti V, Ramanathan S (2009) Electrical triggering of metal-insulator transition in nanoscale vanadium oxide junctions. J Appl Phys 106(8):083702, http://dx.doi.org/10.1063/1.3245338
130. Xue K-H, de Araujo CAP, Celinska J, McWilliams C (2011) A non-filamentary model for unipolar switching transition metal oxide resistance random access memories. J Appl Phys 109(9):091602
131. Meijer G, Staub U, Janousch M, Johnson S, Delley B, Neisius T (2005) Valence states of Cr and the insulator-to-metal transition in Cr-doped $SrTiO_3$. Phys Rev B Condens Matter 72(15):155102
132. Ha SD, Aydogdu GH, Ramanathan S (2011) Metal-insulator transition and electrically driven memristive characteristics of $SmNiO_3$ thin films. Appl Phys Lett 98(1):012105
133. Ohtomo A, Hwang H (2004) A high-mobility electron gas at the $LaAlO_3$/$SrTiO_3$ heterointerface. Nature 427(6973):423–6
134. Thiel S, Hammerl G, Schmehl A, Schneider C, Mannhart J (2006) Tunable quasi-two-dimensional electron gases in oxide heterostructures. Science 313(5795):1942–5
135. Niranjan MK, Wang Y, Jaswal SS, Tsymbal EY (2009) Prediction of a switchable two-dimensional electron gas at ferroelectric oxide interfaces. Phys Rev Lett 103(1):016804
136. Park J, Bogorin D, Cen C, Felker D, Zhang Y, Nelson C et al (2010) Creation of a two-dimensional electron gas at an oxide interface on silicon. Nat Commun 1:94
137. Villena MA, Roldán JB, Jimenez-Molinos F, Suñé J, Long S, Miranda E et al (2014) A comprehensive analysis on progressive reset transitions in RRAMs. J Phys D Appl Phys 47(20):205102. doi:10.1088/0022-3727/47/20/205102
138. Szot K, Rogala M, Speier W, Klusek Z, Besmehn A, Waser R (2011) $TiO_2$—a prototypical memristive material. Nanotechnology 22(25):254001. doi:10.1088/0957-4484/22/25/254001
139. Sacchetto D, De Micheli G, Leblebici Y (2012) Multiterminal memristive nanowire devices for logic and memory applications: a review. Proc IEEE 100(6):2008–20. doi:10.1109/JPROC.2011.2172569

140. Indiveri G, Linares-Barranco B, Legenstein R, Deligeorgis G, Prodromakis T (2013) Integration of nanoscale memristor synapses in neuromorphic computing architectures. Nanotechnology 24(38):384010. doi:10.1088/0957-4484/24/38/384010
141. Sacchetto D, Gaillardon P, Zervas M, Carrara S, De Micheli G, Leblebici Y (2013) Applications of multi-terminal memristive devices: a review. IEEE Circuits Syst Mag 13(2):23–41. doi:10.1109/MCAS.2013.2256258
142. Hu SG, Wu SY, Jia WW, Yu Q, Deng LJ, Fu YQ et al (2014) Review of nanostructured resistive switching memristor and its applications. Nanosci Nanotechnol Lett 6(9):729–57. doi:10.1166/nnl.2014.1888
143. Datta S (1995) Electronic transport in mesoscopic systems. Cambridge University Press, New York
144. Landauer R (1970) Electrical resistance of disordered one-dimensional lattices. Philos Mag 21(172):863–7
145. Scheer E, Agraït N, Cuevas JC, Yeyati AL, Ludoph B, Martín-Rodero A et al (1998) The signature of chemical valence in the electrical conduction through a single-atom contact. Nature 394(6689):154–7
146. Van Wees B, Van Houten H, Beenakker C, Williamson JG, Kouwenhoven L, Van der Marel D et al (1988) Quantized conductance of point contacts in a two-dimensional electron gas. Phys Rev Lett 60(9):848
147. Wharam D, Thornton T, Newbury R, Pepper M, Ahmed H, Frost J et al (1988) One-dimensional transport and the quantisation of the ballistic resistance. J Phys C Solid State Phys 21(8):L209
148. Agrait N, Rodrigo J, Vieira S (1993) Conductance steps and quantization in atomic-size contacts. Phys Rev B Condens Matter 47(18):12345
149. Pascual JI, Méndez J, Gómez-Herrero J, Baró AM, García N, Binh VT (1993) Quantum contact in gold nanostructures by scanning tunneling microscopy. Phys Rev Lett 71(12):1852–5. doi:10.1103/PhysRevLett.71.1852
150. Fendley P, Ludwig AWW, Saleur H (1995) Exact conductance through point contacts in the $\nu = 1/3$ fractional quantum hall effect. Phys Rev Lett 74(15):3005–8. doi:10.1103/PhysRevLett.74.3005
151. Ott F, Barberan S, Lunney J, Coey J, Berthet P, de Leon-Guevara A et al (1998) Quantized conductance in a contact between metallic oxide crystals. Phys Rev B Condens Matter 58(8):4656
152. Yang C-S, Thiltges J, Doudin B, Johnson M (2002) In situ monitoring of quantum conductance in electrodeposited magnetic point contacts. J Phys Condens Matter 14(50):L765
153. Havu P, Puska MJ, Nieminen RM, Havu V. Electron transport through quantum wires and point contacts. Phys Rev B: Condens Matter. 2004; 70(23). doi:10.1103/PhysRevB.70.233308.
154. Vandersypen LMK, Elzerman JM, Schouten RN, Willems van Beveren LH, Hanson R, Kouwenhoven LP (2004) Real-time detection of single-electron tunneling using a quantum point contact. Appl Phys Lett 85(19):4394. doi:10.1063/1.1815041
155. Xie FQ, Nittler L, Obermair C, Schimmel T. Gate-controlled atomic quantum switch. Phys Rev Lett. 2004; 93(12). doi:10.1103/PhysRevLett.93.128303.
156. He J, Sankey O, Lee M, Tao N, Li X, Lindsay S (2006) Measuring single molecule conductance with break junctions. Faraday Discuss 131:145–54. doi:10.1039/b508434m
157. Reed MA, Zhou C, Muller C, Burgin T, Tour J (1997) Conductance of a molecular junction. Science 278(5336):252–4
158. He H, Li C, Tao N (2001) Conductance of polymer nanowires fabricated by a combined electrodeposition and mechanical break junction method. Appl Phys Lett 78(6):811–3
159. Gonzalez JI, Lee T-H, Barnes MD, Antoku Y, Dickson RM (2004) Quantum mechanical single-gold-nanocluster electroluminescent light source at room temperature. Phys Rev Lett 93(14):147402
160. Tian J-H, Liu B, Li X, Yang Z-L, Ren B, Wu S-T et al (2006) Study of molecular junctions with a combined surface-enhanced Raman and mechanically controllable break junction method. J Am Chem Soc 128(46):14748–9
161. Chico L, Benedict LX, Louie SG, Cohen ML (1996) Quantum conductance of carbon nanotubes with defects. Phys Rev B Condens Matter 54(4):2600
162. Frank S (1998) Carbon nanotube quantum resistors. Science 280(5370):1744–6. doi:10.1126/science.280.5370.1744
163. Poncharal P, Wang Z, de Heer W (1999) Conductance quantization in multiwalled carbon nanotubes. Eur Phys J D 9(1):77–9
164. Choi HJ, Ihm J, Louie SG, Cohen ML (2000) Defects, quasibound states, and quantum conductance in metallic carbon nanotubes. Phys Rev Lett 84(13):2917
165. Sanvito S, Kwon Y-K, Tománek D, Lambert CJ (2000) Fractional quantum conductance in carbon nanotubes. Phys Rev Lett 84(9):1974
166. Kong J, Yenilmez E, Tombler TW, Kim W, Dai H, Laughlin RB et al. Quantum interference and ballistic transmission in nanotube electron waveguides. Phys Rev Lett. 2001; 87(10). doi:10.1103/PhysRevLett.87.106801.
167. Urbina A, Echeverría I, Pérez-Garrido A, Díaz-Sánchez A, Abellán J. Quantum conductance steps in solutions of multiwalled carbon nanotubes. Phys Rev Lett. 2003; 90(10). doi:10.1103/PhysRevLett.90.106603.
168. Agraıt N, Yeyati AL, Van Ruitenbeek JM (2003) Quantum properties of atomic-sized conductors. Phys Rep 377(2):81–279
169. Terabe K, Hasegawa T, Nakayama T, Aono M (2005) Quantized conductance atomic switch. Nature 433(7021):47–50
170. Zhu X, Su W, Liu Y, Hu B, Pan L, Lu W et al (2012) Observation of conductance quantization in oxide-based resistive switching memory. Adv Mater 24(29):3941–6. doi:10.1002/adma.201201506
171. Chen C, Gao S, Zeng F, Wang GY, Li SZ, Song C et al (2013) Conductance quantization in oxygen-anion-migration-based resistive switching memory devices. Appl Phys Lett 103(4):043510. doi:10.1063/1.4816747
172. Sakamoto T, Sunamura H, Kawaura H, Hasegawa T, Nakayama T, Aono M (2003) Nanometer-scale switches using copper sulfide. Appl Phys Lett 82(18):3032. doi:10.1063/1.1572964
173. Liao ZM, Hou C, Zhao Q, Wang DS, Li YD, Yu DP (2009) Resistive switching and metallic-filament formation in $Ag_2S$ nanowire transistors. Small 5(21):2377–81. doi:10.1002/smll.200900642
174. Yun E-J, Becker MF, Walser RM (1993) Room temperature conductance quantization in V‖amorphous-V2O5‖V thin film structures. Appl Phys Lett 63(18):2493. doi:10.1063/1.110459
175. Jameson JR, Gilbert N, Koushan F, Saenz J, Wang J, Hollmer S et al (2011) One-dimensional model of the programming kinetics of conductive-bridge memory cells. Appl Phys Lett 99(6):063506. doi:10.1063/1.3623485
176. Xue K-H, Paz de Araujo CA, Celinska J, McWilliams C (2011) A non-filamentary model for unipolar switching transition metal oxide resistance random access memories. J Appl Phys 109(9):091602. doi:10.1063/1.3581193
177. Cartoixà X, Rurali R, Suñé J. Transport properties of oxygen vacancy filaments in metal/crystalline or amorphous $HfO_2$/metal structures. Phys Rev B: Condens Matter. 2012; 86(16). doi:10.1103/PhysRevB.86.165445.
178. Liu X, Liu Y, Chen W, Li J, Liao L (2012) Ferroelectric memory based on nanostructures. Nanoscale Res Lett 7(1):285. doi:10.1186/1556-276X-7-285
179. Miranda E, Kano S, Dou C, Kakushima K, Suñé J, Iwai H (2012) Nonlinear conductance quantization effects in $CeO_X/SiO_2$-based resistive switching devices. Appl Phys Lett 101(1):012910. doi:10.1063/1.4733356
180. Tappertzhofen S, Valov I, Waser R (2012) Quantum conductance and switching kinetics of AgI-based microcrossbar cells. Nanotechnology 23(14):145703. doi:10.1088/0957-4484/23/14/145703
181. Tsuruoka T, Hasegawa T, Terabe K, Aono M (2012) Conductance quantization and synaptic behavior in a $Ta_2O_5$-based atomic switch. Nanotechnology 23(43):435705. doi:10.1088/0957-4484/23/43/435705
182. Wagenaar JJT, Morales-Masis M, van Ruitenbeek JM (2012) Observing “quantized” conductance steps in silver sulfide: Two parallel resistive switching mechanisms. J Appl Phys 111(1):014302. doi:10.1063/1.3672824
183. Gao S, Zeng F, Chen C, Tang G, Lin Y, Zheng Z et al (2013) Conductance quantization in a Ag filament-based polymer resistive memory. Nanotechnology 24(33):335201. doi:10.1088/0957-4484/24/33/335201
184. Ielmini D, Cagli C, Nardi F, Zhang Y (2013) Nanowire-based resistive switching memories: devices, operation and scaling. J Phys D Appl Phys 46(7):074006. doi:10.1088/0022-3727/46/7/074006
185. Liu D, Cheng H, Zhu X, Wang G, Wang N (2013) Analog memristors based on thickening/thinning of Ag nanofilaments in amorphous manganite thin films. ACS Appl Mater Interfaces 5(21):11258–64. doi:10.1021/am403497y
186. Mehonic A, Vrajitoarea A, Cueff S, Hudziak S, Howe H, Labbe C et al (2013) Quantum conductance in silicon oxide resistive memory devices. Sci Rep 3:2708. doi:10.1038/srep02708
187. Saura X, Miranda E, Jiménez D, Long S, Liu M, Rafí JM et al (2013) Threshold switching and conductance quantization in Al/$HfO_2$/Si(p) structures. Jpn J Appl Phys 52(4S):04CD6. doi:10.7567/jjap.52.04cd06
188. Syu Y-E, Chang T-C, Lou J-H, Tsai T-M, Chang K-C, Tsai M-J et al (2013) Atomic-level quantized reaction of $HfO_X$ memristor. Appl Phys Lett 102(17):172903. doi:10.1063/1.4802821
189. Hu C, McDaniel MD, Posadas A, Demkov AA, Ekerdt JG, Yu ET (2014) Highly controllable and stable quantized conductance and resistive switching

mechanism in single-crystal $TiO_2$ resistive memory on silicon. Nano Lett 14(8):4360–7. doi:10.1021/nl501249q
190. Lv H, Xu X, Sun P, Liu H, Luo Q, Liu Q et al (2015) Atomic view of filament growth in electrochemical memristive elements. Sci Rep 5:13311. doi:10.1038/srep13311
191. Geresdi A, Halbritter A, Gyenis A, Makk P, Mihály G (2011) From stochastic single atomic switch to nanoscale resistive memory device. Nanoscale 3(4):1504–7
192. Hajto J, Rose MJ, Snell AJ, Osborne IS, Owen AE, Lecomber PG. Quantised electron effects in metal/a-Si:H/metal thin film structures. J Non-Cryst Solids. 1991;137–138, Part 1(0):499–502. http://dx.doi.org/10.1016/S0022-3093(05)80164-4.
193. Jameson JR, Gilbert N, Koushan F, Saenz J, Wang J, Hollmer S et al (2012) Quantized conductance in Ag/$GeS_2$/W conductive-bridge memory cells. IEEE Electron Device Lett 33(2):257–9
194. Hu C, McDaniel MD, Ekerdt JG, Yu ET (2013) High ON/OFF ratio and quantized conductance in resistive switching of on silicon. IEEE Electron Device Lett 34(11):1385–7
195. Tappertzhofen S, Linn E, Menzel S, Kenyon AJ, Waser R, Valov I (2015) Modeling of quantized conductance effects in electrochemical metallization cells. IEEE Trans Nanotechnol 14(3):505–12. doi:10.1109/TNANO.2015.2411774
196. Van KAMPENNG (1976) The expansion of the master equation. Adv Chem Phys 34:245–309. doi:10.1002/9780470142530.ch5
197. Xia J-B (1992) Quantum waveguide theory for mesoscopic structures. Phys Rev B Condens Matter 45(7):3593–9. doi:10.1103/PhysRevB.45.3593
198. Landauer R (1957) Spatial variation of currents and fields due to localized scatterers in metallic conduction. IBM J Res Dev 1(3):223–31
199. Büttiker M, Imry Y, Landauer R, Pinhas S (1985) Generalized many-channel conductance formula with application to small rings. Phys Rev B Condens Matter 31(10):6207–15. doi:10.1103/PhysRevB.31.6207
200. Landauer R (1989) Conductance determined by transmission: probes and quantised constriction resistance. J Phys Condens Matter 1(43):8099
201. Ciraci S, Tekman E (1989) Theory of transition from the tunneling regime to point contact in scanning tunneling microscopy. Phys Rev B Condens Matter 40(17):11969–72. doi:10.1103/PhysRevB.40.11969
202. Brandbyge M, Schiøtz J, Sørensen MR, Stoltze P, Jacobsen KW, Nørskov JK et al (1995) Quantized conductance in atom-sized wires between two metals. Phys Rev B Condens Matter 52(11):8499–514. doi:10.1103/PhysRevB.52.8499
203. Milliken F, Umbach C, Webb R (1996) Indications of a Luttinger liquid in the fractional quantum Hall regime. Solid State Commun 97(4):309–13
204. Brandbyge M, Jacobsen KW, Nørskov JK (1997) Scattering and conductance quantization in three-dimensional metal nanocontacts. Phys Rev B Condens Matter 55(4):2637
205. Mozos J-L, Wan C, Taraschi G, Wang J, Guo H (1997) Quantized conductance of Si atomic wires. Phys Rev B Condens Matter 56(8):R4351
206. Lang N, Avouris P (1998) Oscillatory conductance of carbon-atom wires. Phys Rev Lett 81(16):3515
207. Brandbyge M, Sørensen MR, Jacobsen KW (1997) Conductance eigenchannels in nanocontacts. Phys Rev B Condens Matter 56(23):14956
208. Todorov T, Sutton A (1993) Jumps in electronic conductance due to mechanical instabilities. Phys Rev Lett 70(14):2138
209. García-Martín A, Torres J, Sáenz J (1996) Finite size corrections to the conductance of ballistic wires. Phys Rev B Condens Matter 54(19):13448
210. Lang N (1995) Resistance of atomic wires. Phys Rev B Condens Matter 52(7):5335
211. Maslov DL, Stone M (1995) Landauer conductance of Luttinger liquids with leads. Phys Rev B Condens Matter 52(8):R5539–R42. doi:10.1103/PhysRevB.52.R5539
212. Miranda EA, Walczyk C, Wenger C, Schroeder T (2010) Model for the resistive switching effect in MIM structures based on the transmission properties of narrow constrictions. IEEE Electron Device Lett 31(6):609–11
213. Tappertzhoven S, Linn E, Menzel S, Waser R, Valov I. Quantum size effects and non-equilibrium states in nanoscale silicon dioxide based resistive switches. IEEE Silicon Nanoelectronic Workshop; Jun 8–10 Honolulu, Hawaii, USA 2014.
214. Miranda E, Sune J (2001) Analytic modeling of leakage current through multiple breakdown paths in $SiO_2$ films. IEEE International Reliability Physics Symposium
215. Zhang M, Long S, Wang G, Xu X, Li Y, Liu Q et al (2014) Set statistics in conductive bridge random access memory device with Cu/$HfO_2$/Pt structure. Appl Phys Lett 105(19):193501. doi:10.1063/1.4901530
216. Shibing L, Xiaojuan L, Cagli C, Perniola L, Miranda E, Ming L et al (2013) A model for the set statistics of RRAM inspired in the percolation model of oxide breakdown. IEEE Electron Device Lett 34(8):999–1001. doi:10.1109/LED.2013.2266332
217. Degraeve R, Goux L, Clima S, Govoreanu B, Chen YY, Kar GS et al (2012) Modeling and tuning the filament properties in RRAM metal oxide stacks for optimized stable cycling. IEEE International Symposium on VLSI Technology, Systems, and Applications (VLSI-TSA)
218. Degraeve R, Roussel P, Goux L, Wouters D, Kittl J, Altimime L et al (2010) Generic learning of TDDB applied to RRAM for improved understanding of conduction and switching mechanism through multiple filaments. IEEE International Electron Devices Meeting (IEDM)
219. Zhang M, Wang G, Long S, Yu Z, Li Y, Xu D et al. Unpublished: a physical model for the statistics of set switching time of resistive RAM measured by width-adjusting pulse operation method (accepted, manuscript ID: EDL-2015-07-1267.R3.). IEEE Electron Device Lett. 2015.
220. Bauer U, Yao L, Tan AJ, Agrawal P, Emori S, Tuller HL et al (2015) Magneto-ionic control of interfacial magnetism. Nature Mater 14(2):174–81. doi:10.1038/nmat4134
221. Valov I, Linn E, Tappertzhofen S, Schmelzer S, van den Hurk J, Lentz F et al (2013) Nanobatteries in redox-based resistive switches require extension of memristor theory. Nat Commun 4:1771. doi:10.1038/ncomms2784
222. Lv H, Xu X, Liu H, Liu R, Liu Q, Banerjee W et al. Evolution of conductive filament and its impact on reliability issues in oxide-electrolyte based resistive random access memory. Sci Rep. 2015; 5. doi:10.1038/srep07764
223. Wang M, Bi C, Li L, Long S, Liu Q, Lv H et al (2014) Thermoelectric Seebeck effect in oxide-based resistive switching memory. Nat Commun 5:4598
224. Rahaman SZ, Maikap S, Chiu H-C, Lin C-H, Wu T-Y, Chen Y-S et al (2010) Bipolar resistive switching memory using Cu metallic filament in $Ge_{0.4}Se_{0.6}$ solid electrolyte. Electrochem Solid-State Lett 13(5):H159–H62
225. Kaeriyama S, Sakamoto T, Sunamura H, Mizuno M, Kawaura H, Hasegawa T et al (2005) A nonvolatile programmable solid-electrolyte nanometer switch. IEEE J Solid State Circuits 40(1):168–76. doi:10.1109/JSSC.2004.837244
226. Schoen DT, Xie C, Cui Y (2007) Electrical switching and phase transformation in silver selenide nanowires. J Am Chem Soc 129(14):4116. doi:10.1021/ja068365s
227. Schindler C, Szot K, Karthäuser S, Waser R (2008) Controlled local filament growth and dissolution in Ag–Ge–Se. physica status solidi (RRL). Rapid Res Lett 2(3):129–31. doi:10.1002/pssr.200802054
228. Guo HX, Yang B, Chen L, Xia YD, Yin KB, Liu ZG et al. Resistive switching devices based on nanocrystalline solid electrolyte $(AgI)_{0.5}(AgPO3)_{0.5}$. Appl Phys Lett. 2007; 91(24). doi:10.1063/1.2825273.
229. Wang Y, Liu Q, Long S, Wang W, Wang Q, Zhang M et al. Investigation of resistive switching in Cu-doped $HfO_2$ thin film for multilevel non-volatile memory applications. Nanotechnology. 2010; 21(4). doi:10.1088/0957-4484/21/4/045202.
230. Zhang M, Long S, Wang G, Liu R, Xu X, Li Y et al (2014) Statistical characteristics of reset switching in Cu/$HfO_2$/Pt resistive switching memory. Nanoscale Res Lett 9:694
231. Guan W, Long S, Liu Q, Liu M, Wang W (2008) Nonpolar nonvolatile resistive switching in Cu doped $ZrO_2$. IEEE Electron Device Lett 29(5):434–7. doi:10.1109/LED.2008.919602
232. Sun J, Liu Q, Xie H, Wu X, Xu F, Xu T et al (2013) In situ observation of nickel as an oxidizable electrode material for the solid-electrolyte-based resistive random access memory. Appl Phys Lett 102(5):053502, http://dx.doi.org/10.1063/1.4790837
233. Schindler C, Thermadam SCP, Waser R, Kozicki MN (2007) Bipolar and unipolar resistive switching in Cu-doped $SiO_2$. IEEE Trans Electron Devices 54(10):2762–8. doi:10.1109/TED.2007.904402
234. Kozicki MN, Gopalan C, Balakrishnan M, Mitkova M (2006) A low-power nonvolatile switching element based on copper-tungsten oxide solid electrolyte. IEEE Trans Nanotechnol 5(5):535–44. doi:10.1109/TNANO.2006.880407
235. Sakamoto T, Banno N, Iguchi N, Kawaura H, Sunamura H, Fujieda S et al (2007) A $Ta_2O_5$ solid-electrolyte switch with improved reliability. IEEE International Symposium on VLSI Technology, Systems, and Applications (VLSI-TSA)
236. Aratani K, Ohba K, Mizuguchi T, Yasuda S, Shiimoto T, Tsushima T et al (2007) A novel resistance memory with high scalability and nanosecond switching. IEEE International Electron Devices Meeting (IEDM)

237. Shibing L, Xiaojuan L, Tianchun Y, Cagli C, Perniola L, Miranda E et al (2013) Cycle-to-cycle intrinsic RESET statistics in $HfO_2$ based unipolar RRAM devices. IEEE Electron Device Lett 34(5):623–5. doi:10.1109/LED.2013.2251314
238. Jung K, Seo H, Kim Y, Im H, Hong J, Park J-W et al (2007) Temperature dependence of high- and low-resistance bistable states in polycrystalline NiO films. Appl Phys Lett 90(5):052104, http://dx.doi.org/10.1063/1.2437668
239. Jung R, Lee M-J, Seo S, Kim DC, Park G-S, Kim K et al (2007) Decrease in switching voltage fluctuation of Pt / $NiO_X$ / Pt structure by process control. Appl Phys Lett 91(2):022112. doi:10.1063/1.2755712
240. Yun J-B, Kim S, Seo S, Lee M-J, Kim D-C, Ahn S-E et al (2007) Random and localized resistive switching observation in Pt/NiO/Pt. physica status solidi (RRL). Rapid Res Lett 1(6):280–2. doi:10.1002/pssr.200701205
241. Long S, Cagli C, Ielmini D, Liu M, Sune J (2011) Reset statistics of NiO-based resistive switching memories. IEEE Electron Device Lett 32(11):1570–2. doi:10.1109/LED.2011.2163613
242. Russo U, Ielmini D, Cagli C, Lacaita AL (2009) Filament conduction and reset mechanism in NiO-based resistive-switching memory (RRAM) devices. IEEE Trans Electron Devices 56(2):186–92. doi:10.1109/TED.2008.2010583
243. Cagli C, Nardi F, Ielmini D (2009) Modeling of set/reset operations in NiO-based resistive-switching memory devices. IEEE Trans Electron Devices 56(8):1712–20. doi:10.1109/TED.2009.2024046
244. Ielmini D, Nardi F, Cagli C (2011) Physical models of size-dependent nanofilament formation and rupture in NiO resistive switching memories. Nanotechnology 22(25):254022. doi:10.1088/0957-4484/22/25/254022
245. Shima H, Takano F, Akinaga H, Tamai Y, Inoue IH, Takagi H (2007) Resistance switching in the metal deficient-type oxides: NiO and CoO. Appl Phys Lett 91(1):012901–3
246. Yasuhara R, Fujiwara K, Horiba K, Kumigashira H, Kotsugi M, Oshima M et al (2009) Inhomogeneous chemical states in resistance-switching devices with a planar-type Pt/CuO/Pt structure. Appl Phys Lett 95(1):012110
247. Inoue IH, Yasuda S, Akinaga H, Takagi H (2008) Nonpolar resistance switching of metal/binary-transition-metal oxides/metal sandwiches: homogeneous/inhomogeneous transition of current distribution. Phys Rev B Condens Matter 77(3):035105

**Submit your manuscript to a SpringerOpen journal and benefit from:**

► Convenient online submission
► Rigorous peer review
► Immediate publication on acceptance
► Open access: articles freely available online
► High visibility within the field
► Retaining the copyright to your article

**Submit your next manuscript at ► springeropen.com**